ACS NANO

www.acsnano.org

ARTICLE

Defective RuO_2 Nanospheres Attenuate Osteoarthritis Progression via Suppressing the ROS/NLRP3/Caspase-1 Signaling Pathway

Jie Lv,[○] Faheem Muhammad,[○] Zheng Wang, Chenfeng Qiao, Xiang Gu, Yuan Liu, Weitong Li, Wenli Gong, Zhongyang Lv, Yuxiang Fei, Liqian Peng, Zhihao Lu, Nuo Xu, Chunqing Hu, Hanwen Zhang, Rui Wu, Xingquan Xu, Hui Wei,* Ziying Sun,* and Dongquan Shi*

Cite This: *ACS Nano* 2025, 19, 23080−23095

Read Online

ACCESS | Metrics & More | Article Recommendations | Supporting Information

ABSTRACT: **Osteoarthritis (OA) is the most prevalent degenerative joint disorder, characterized by chronic inflammation, cartilage degeneration, and the formation of osteophytes, which leads to serious economic and social challenges. Previous studies have demonstrated that oxidative stress-driven inflammation plays a crucial role in the pathophysiological progression of OA. In this study, we presented defective RuO_2 (d-RuO_2) as an effective antioxidant for the treatment of OA. Unlike the crystalline RuO_2, the amorphous hydrous RuO_2 nanospheres (composed of self-assembled ultrasmall RuO_2) displayed superior nanozymatic antioxidant activities. *In vitro* studies demonstrated that d-RuO_2 significantly reduced intracellular levels of reactive oxygen species (ROS), and decreased the expression of key inflammatory markers including inducible nitric oxide synthase (iNOS), cyclooxygenase-2 (COX2), tumor necrosis factor-α (TNF-α), and interleukin-1β (IL-1β), indicating its anti-inflammatory effects. *In vivo* experiments showed that d-RuO_2 effectively relieved pain, improved physical activity, and mitigated synovitis, cartilage degeneration, and bone remodeling induced by destabilization of the medial meniscus (DMM). Furthermore, the mechanistic investigations indicated that d-RuO_2 attenuated the progression of OA by suppressing the ROS/NLRP3/Caspase-1 signaling pathway. In conclusion, we presented d-RuO_2 as an efficient ROS scavenger, providing a potential therapeutic strategy for OA.**

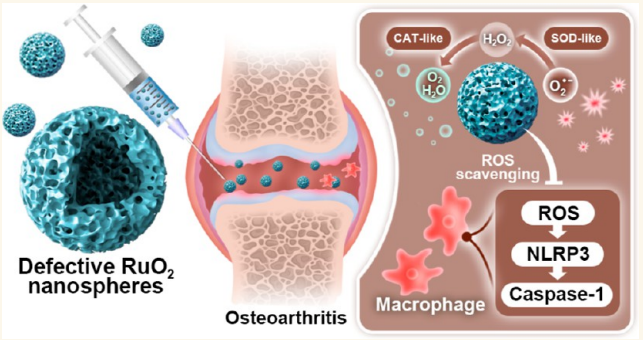

KEYWORDS: *defective RuO_2, nanozyme, osteoarthritis, reactive oxygen species, NLRP3*

Osteoarthritis (OA) is the most common degenerative joint condition characterized by synovitis, cartilage degeneration, and osteophyte formation.[1−3] Approximately 7% of the global population suffers from OA, resulting in great social and economic burdens.[4] Surgery is an effective treatment option for end-stage osteoarthritis when conservative measures fail to provide relief. Until now, there is still no effective method to attenuate the progression of OA. Knee osteoarthritis (KOA) is the most common form of OA in the lower extremities.[5] KOA can be classified into several stages: pre-KOA, early KOA, progressive KOA, and end-stage KOA. Progressive KOA can be further divided into four subtypes: cartilage degradation-driven, bone remodeling-driven, inflammation-driven, and pain-driven subtype.[6] In inflammation-driven OA, the production and release of inflammatory factors and matrix hydrolases, such as interleukin-1β (IL-1β), tumor necrosis factor-α (TNF-α), and matrix metallopeptidase 13 (MMP13), can trigger an inflammatory cascade response, further exacerbating the progression of OA.[7] Although the underlying pathogenesis remains unclear, studies revealed that oxidative stress-induced inflammation participates in the OA progression.[8] Oxidative stress results from an imbalance between the generation and clearance of reactive oxygen species (ROS).[9] The imbalance often leads to increased expression of inflammatory cytokines and chemokines, and ultimately leads to cell damage and apoptosis.[10] ROS overproduction activates NOD-like receptor protein 3 (NLRP3), which mediates

Received: March 6, 2025
Revised: June 2, 2025
Accepted: June 3, 2025
Published: June 20, 2025

https://doi.org/10.1021/acsnano.5c04011
ACS Nano 2025, 19, 23080−23095

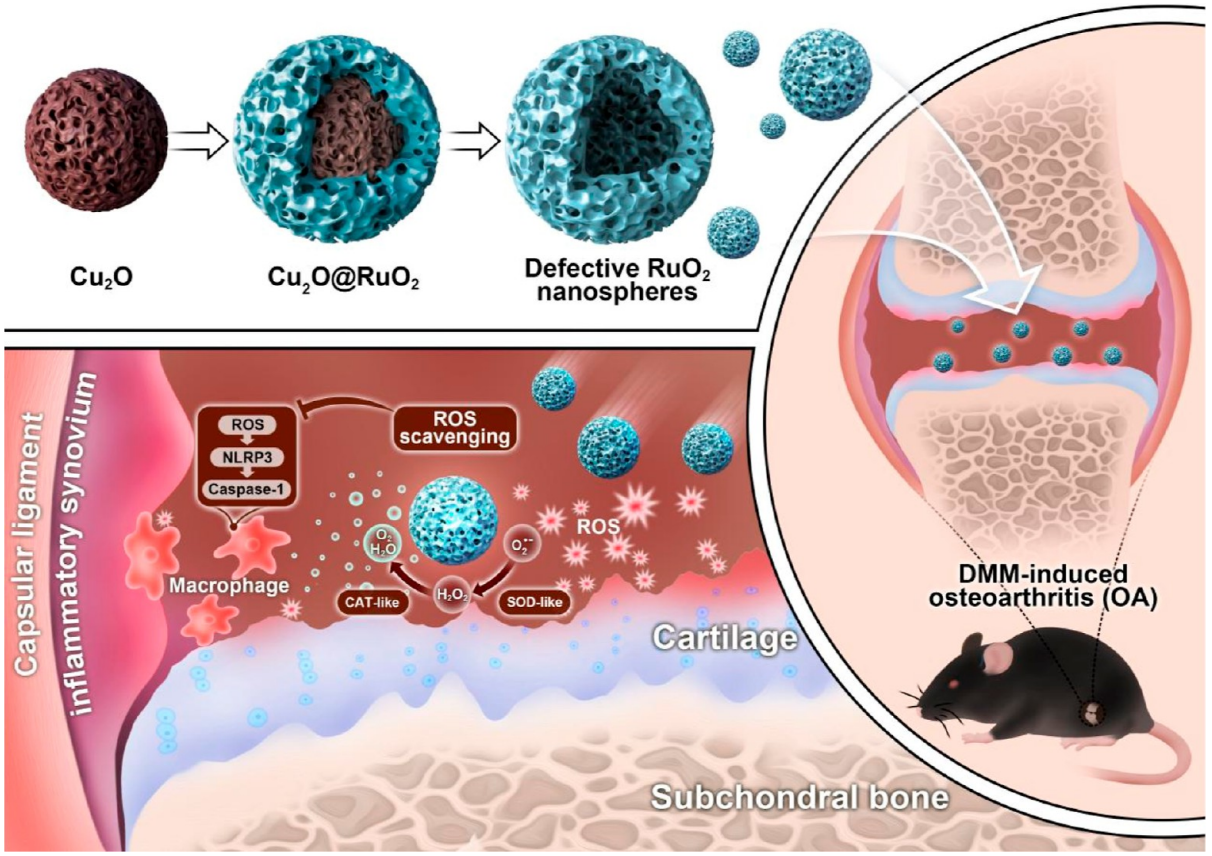

Figure 1. A schematic diagram demonstrating the synthetic route of defective RuO_2 nanospheres and showing the working mechanism to attenuate osteoarthritis progression by suppressing ROS/NLRP3/Caspase-1 signaling pathway.

activation of caspase-1 and the subsequent release of proinflammatory cytokines IL-1β/IL-18 in response to microbial infections and cellular damage.[11−13] Therefore, antioxidant therapy is essential for reversing the progression of OA.

Nanozymes are nanomaterials with intrinsic enzyme-like activities.[14] Nanozymes offer numerous advantages, including multienzyme-like activities, simple synthetic protocols, high stability, and low cost over natural enzymes. They can effectively catalyze different oxidoreductase substrates while exhibiting catalytic efficiency and reaction kinetics similar to those of natural enzymes.[15−17] They have been widely explored in various biomedical applications due to their favorable biological properties, including detection, imaging, and therapies.[18,19] The levels of ROS in cells are regulated by superoxide dismutase (SOD) and catalase (CAT) enzymes, which convert into harmless water and oxygen.[7] Certain nanozymes exhibit SOD-like and CAT-like activities, enabling them to be used for the elimination of excessive intracellular ROS,[20,21] offering a therapeutic approach for the treatment of OA. Several metal oxides have been tested as antioxidant nanozymes, including Mn_3O_4, MnO_2, V_2O_5, Fe_3O_4, MoO_2, Cu_2O, Fe_2O_3, *etc.*[14,22] Given the instability and toxicity of the previously explored metal oxides, ruthenium dioxide (RuO_2) is an emerging metal oxide-based nanozyme that exhibits excellent biocatalytic activities and a biosafety profile.[23] In particular, it has been demonstrated that ruthenium-centered nanomaterials show exceptionally high CAT-like activities relative to natural antioxidants and recently reported ROS scavenging nanozymes.[23−26] Until now, RuO_2 has mostly been used as individual nanoparticles, which tend to aggregate and display lower stability. Compared to single nanoparticles or solid spheres, hollow structures offer unique properties including low density, functional walls, availability of pores and cavities, abundant active sites, and easy mass transfer, and exchange.[27−29]

In this study, we have thus synthesized hollow-structured defective RuO_2 (d-RuO_2) using a template-mediated approach and explored it in the treatment of OA. Hollow RuO_2 nanospheres exhibited significant antioxidant properties in both *in vitro* and *in vivo* studies. In cellular experiments, d-RuO_2 decreased the level of ROS and the expression of inflammatory markers in macrophages. Hollow d-RuO_2 notably attenuated the progression of OA in mouse models induced by surgical destabilization of the medial meniscus (DMM), we observed improved mobility and alleviation of OA pathologic progression in DMM mice. Detailed mechanistic investigation revealed that RuO_2 nanozyme diminished the progression of OA by suppressing the ROS/NLRP3/Caspase-1 signaling pathway (Figure 1).

RESULTS AND DISCUSSION

Synthesis and Characterization of d-RuO_2. The amorphous RuO_2 antioxidant nanozyme was produced using Cu_2O nanospheres as a reactive template. The exposure of aqueous solution of ruthenium chloride to Cu_2O led to the spontaneous growth of amorphous ultrasmall RuO_2 nanoparticles onto the surface of Cu_2O nanospheres. Given the toxicity of copper, the as-synthesized core−shell nanostructure (Cu_2O@d-RuO_2) was subsequently treated with aqueous ammonia solution to etch the Cu_2O core. Following the

https://doi.org/10.1021/acsnano.5c04011
ACS Nano 2025, 19, 23080−23095

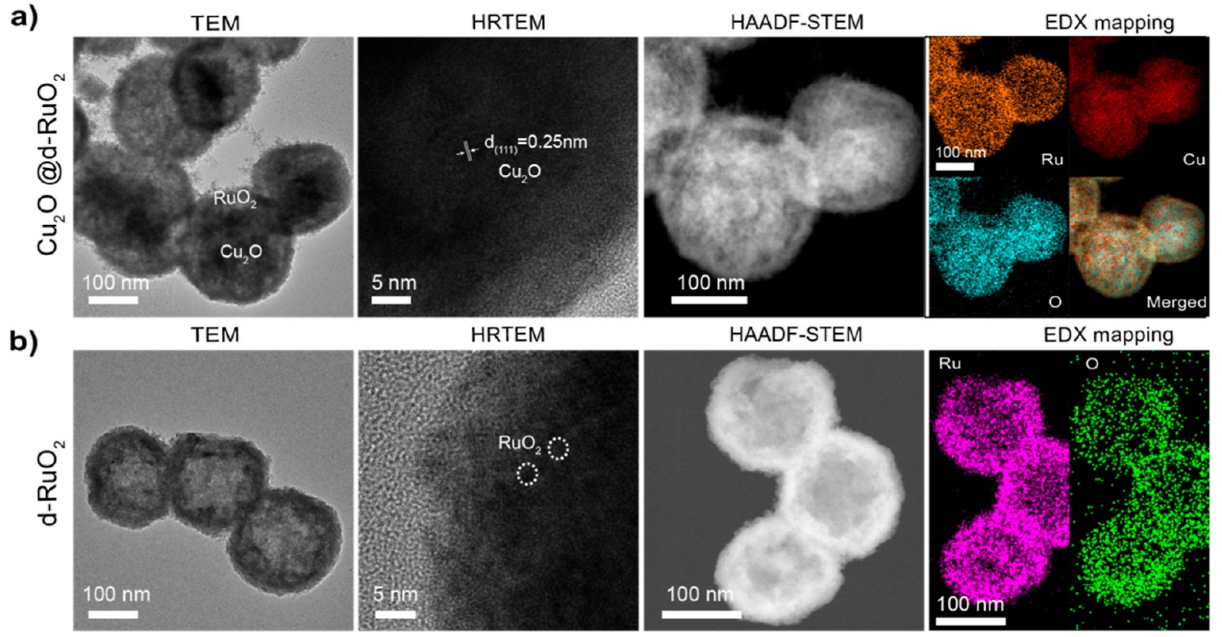

Figure 2. Electron microscopic characterization to track the synthetic route in the formation of d-RuO_2 nanospheres. (a) TEM, HRTEM, STEM, and EDX elemental mapping images of intermediate Cu_2O@d-RuO_2 core−shell nanostructures. (b) TEM, HRTEM, STEM, and EDX elemental mapping images of desired hollow d-RuO_2 nanospheres.

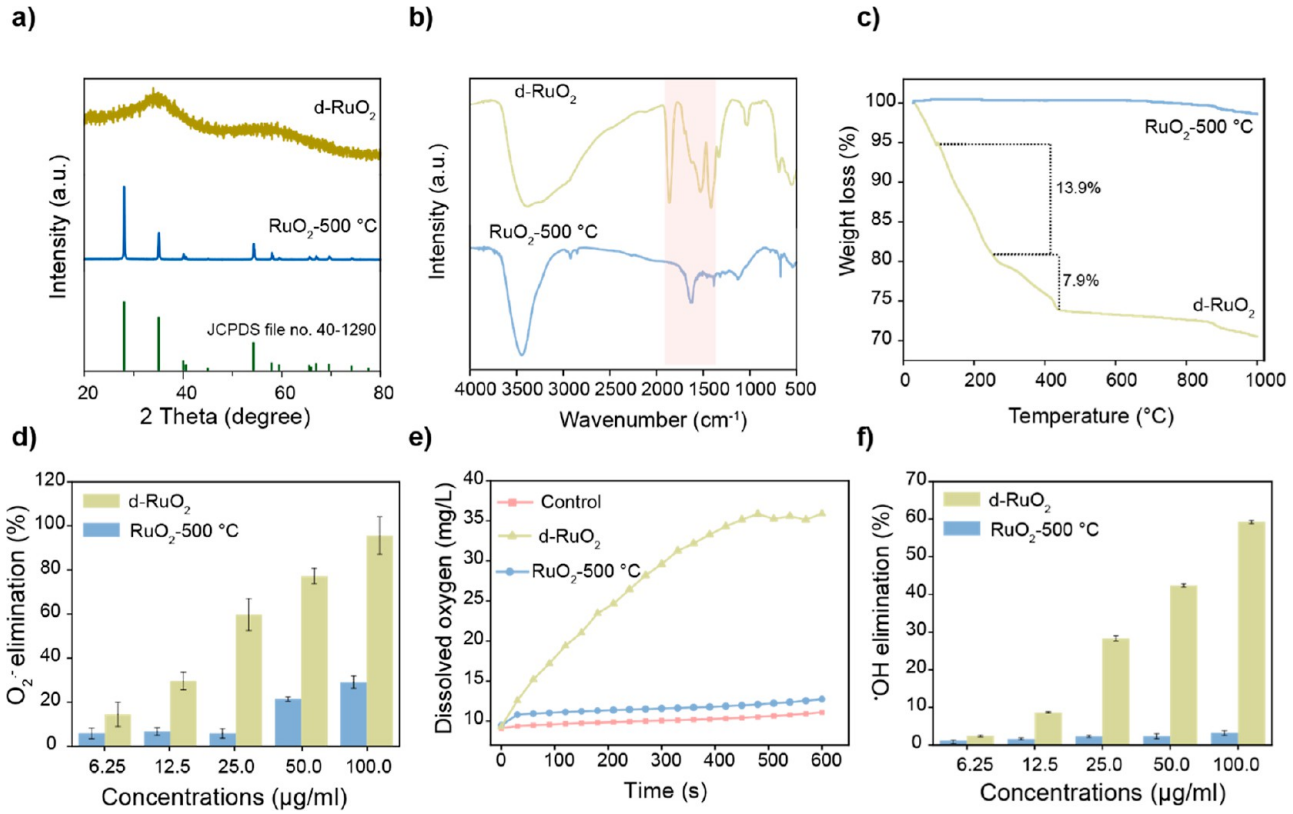

Figure 3. Structural characterization and nanozymatic performance of defective and thermally treated RuO_2 nanostructures. (a) Powder XRD patterns of defective and thermally treated RuO_2 nanostructures. (b) FTIR spectra of PVP-capped defective and thermally treated RuO_2 nanospheres. (c) TGA thermograms of defective and thermally treated RuO_2 nanospheres. (d−f) SOD-like, CAT-like, and hydroxyl radicals quenching activities of both defective and thermally treated RuO_2 nanostructures. Data are shown as mean ± SD (n = 3).

etching treatment, we obtained the required hollow d-RuO_2 nanospheres. Different electron microscopic techniques including scanning electron microscopy (SEM), transmission electron microscopy (TEM), and high-angle annular dark-field scanning transmission electron microscopy (HAADF-STEM) were conducted to determine the morphology, structure, crystallinity, and elemental compositions of various nanostructures involved during the synthesis of d-RuO_2 nanospheres.

https://doi.org/10.1021/acsnano.5c04011
ACS Nano 2025, 19, 23080−23095

Figure S1 schematically illustrates the synthetic protocol and the respective SEM images of the Cu_2O template, core−shelled Cu_2O@d-RuO_2, and hollow d-RuO_2 nanospheres. SEM analysis indicates monodispersed Cu_2O with a spherical morphology (particle size was ∼250 nm); the subsequently formed d-RuO_2 containing nanostructures also notably retained the morphology and size, as was found in the parent Cu_2O template. Unlike the surface observed in parent Cu_2O, more roughened and dotted surfaces can be seen in core−shelled Cu_2O@d-RuO_2 and hollow d-RuO_2 nanostructures. The low-resolution and HRTEM images reveal the structure and the polycrystalline nature of Cu_2O (Figure S2). The inspection of Cu_2O@d-RuO_2 reveals a core−shelled nanostructure composed of a darker crystalline core of Cu_2O and a porous amorphous RuO_2 shell, as shown in Figure 2a. As can be seen in the HAADF-STEM image, the core−shell nanostructure consists of two different phases with darker and lighter contrast: a relatively darker outer contrast indicates the presence of amorphous RuO_2, whereas a lighter inner contrast shows the crystalline Cu_2O core. The energy-dispersive X-ray (EDX) elemental mapping of the Cu_2O@RuO_2 also verified the core−shelled nanostructure. After etching the superfluous Cu_2O core, we obtained the desired d-RuO_2 nanospheres. The low-resolution TEM image in Figure 2b shows the well-defined hollow RuO_2 nanostructures, while the examination at higher resolution indicates that the shell of the hollow nanospheres was actually formed by self-assembly of ultrasmall RuO_2 (∼2 nm). The absence of lattice fringes in d-RuO_2 corroborated the amorphous nature of ultrasmall RuO_2. The compositional map shows the atomic distribution of ruthenium and oxygen in d-RuO_2. The obtained hollow d-RuO_2 sample was also thermally treated at 500 °C and its structural transformation was examined by TEM. Figure S3 indicates the aggregation of the d-RuO_2 sample following thermal treatment, and at the same time, a phase transformation was also observed. The disordered RuO_2 nanosphere was changed into a well-crystalline phase, polycrystalline RuO_2-500 °C (50−100 nm) can be seen in the HRTEM image.

The disordered or crystalline nature of RuO_2 samples was analyzed by X-ray powder diffraction (XRD). We did not observe any well-defined RuO_2-associated peaks, the absence of peaks implied the amorphous/defective nature of the as-synthesized RuO_2 (Figure 3a). On the other hand, thermally treated RuO_2 showed sharp characteristic peaks of rutile-phase RuO_2 (JCPDS file no. 40-1290), suggesting that a phase transformation occurred in the RuO_2-500 °C sample. X-ray photoelectron spectroscopy (XPS) probed RuO_2's surface composition, oxidation states, and hydrous nature. Due to the overlap of the XPS signals of Ru 3d photoelectrons with those of C 1s, we analyzed the Ru 3p core-line spectrum. As shown in Figure S4a, the deconvoluted spectrum revealed four peaks: two peaks at 463.3 and 485.5 eV were linked to tetravalent ruthenium, whereas the other two less pronounced peaks at 465.2 and 487.3 eV were associated with trivalent ruthenium. The deconvoluted O 1s spectrum of d-RuO_2 showed three discrete components corresponding to lattice oxygen, hydroxyl groups, and confined water content, as shown in Figure S4b.[30] These findings implied that the as-synthesized d-RuO_2 possesses a considerable amount of trivalent hydrated species (Ru−O−H). Curve fitting of Ru 3p and O 1s core level peaks was also performed for thermally treated RuO_2 sample to evaluate the concentration of trivalent ruthenium and confined water content in RuO_2-500 °C. Figure S5 indicates a relatively lower trivalent ruthenium content in the thermally treated sample than in the hydrous RuO_2. Moreover, a more pronounced lattice oxygen (Ru−O−Ru) component could also be seen, implying the transformation of amorphous hydrous RuO_2 into a tetravalent crystalline product. The FTIR absorption spectra of RuO_2 samples were obtained to identify the presence of surface-bound PVP. Figure 3b substantiated the presence of PVP-associated peaks in as-synthesized RuO_2. Upon thermal treatment at 500 °C, the organic molecules present on the surface of as-synthesized RuO_2 were burnt out, as indicated by the diminishing of PVP-related peaks. To determine the water content in the as-synthesized RuO_2, thermogravimetric analysis (TGA) was performed in the air atmosphere (heating rate 10 °C/min). As shown in Figure 3c, a more significant weight loss (13.9%) was observed from 100 to 250 °C, then a gradual decomposition (7.9%) from 250 to 440 °C. The initial loss could be ascribed to dehydration, while the second loss could be associated with chemical dehydration and decomposition of organic molecules. On the contrary, a nonsignificant weight loss from 100 to 700 °C in a thermally treated sample (RuO_2-500 °C) was observed, representing the lack of confined water and the crystalline nature of the sample, as noticed in the XRD and HRTEM results. Raman spectroscopy also revealed the defective crystal structure of as-synthesized RuO_2 relative to a thermally treated sample. The pronounced Raman peaks located at 513, 625, and 695 cm^{-1} were observed in RuO_2-500 °C corresponding to the E_g, A_{1g}, and B_{2g} modes, respectively. Comparatively, broader and weaker Raman-active modes were observed in as-synthesized RuO_2, signifying the local lattice defectiveness and short-range order (Figure S6).

The antioxidant nanozymatic potential of both RuO_2 samples was gauged by determining the superoxide dismutase (SOD)-like, catalase (CAT)-like, and hydroxyl radicals quenching activities. WST-1 kit was used to evaluate the quenching of superoxide ($O_2^{\bullet-}$) species. The different concentrations of d-RuO_2 nanospheres were exposed to in situ generated $O_2^{\bullet-}$. As low as 25 μg/mL of d-RuO_2 scavenged ∼60% of the reactive radicals, as shown in Figure 3d. On the contrary, very poor SOD-like activity was observed in the RuO_2-500 °C sample, most likely due to the completely oxidized and crystalline crystal structure. Using an oxygen meter, we quantified the catalytic decomposition of H_2O_2 onto the surface of RuO_2 samples. A significantly high CAT-like activity was witnessed in d-RuO_2 nanospheres, which agrees with our previous report that the CAT-like activity of hydrous RuO_2 is as high as displayed by benchmark Pt.[31] However, the CAT-like activity exhibited by RuO_2-500 °C was found to be negligible (Figure 3e). Hydroxyl radicals ($^{\bullet}OH$) are the most toxic reactive entities in the biological domain, $^{\bullet}OH$ scavenging capacities of d-RuO_2 nanospheres were also tested using Griess reagent. As shown in Figure 3f, RuO_2-500 °C failed to achieve the scavenging of $^{\bullet}OH$, whereas a dose-dependent quenching of $^{\bullet}OH$ was noticed in the case of d-RuO_2. The appreciable antioxidant nanozymatic activities of d-RuO_2 inspired us to explore it for the treatment of OA.

Biocompatibility and *In Vivo* Metabolism of d-RuO_2 Nanozyme. First, we explored the biocompatibility of d-RuO_2 nanozyme at both cellular and animal levels. In *in vitro* cellular experiments, we cocultured RAW264.7 macrophages, SW982 cells, and chondrocytes with d-RuO_2 nanozyme at concentrations ranging from 0 μg/mL to 100 μg/mL, and

https://doi.org/10.1021/acsnano.5c04011
ACS Nano 2025, 19, 23080−23095

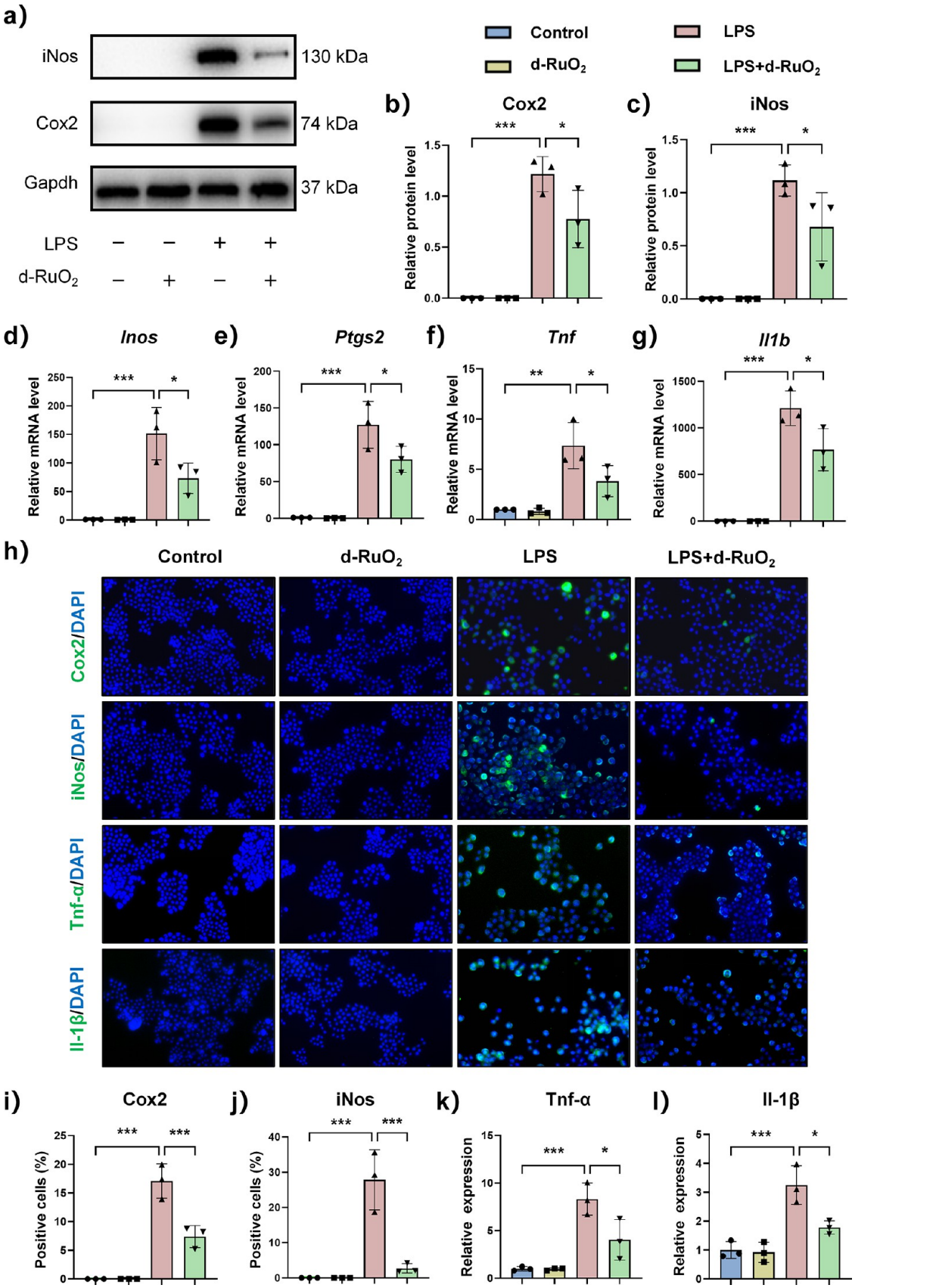

Figure 4. Defective RuO_2 nanozyme inhibits macrophagic inflammation induced by LPS *in vitro*. (a) Representative Western blot images of Cox2, iNos, and Gapdh expression in RAW264.7 macrophages after LPS stimulation with or without d-RuO_2 nanozyme treatment for 36 h. (b,c) Quantification of relative protein level of Cox2 (b) and iNos (c). (d−g) qPCR analysis of relative mRNA level of *Inos* (d), *Ptgs2* (e), *Tnf* (f), and *Il1b* (g) in RAW264.7 macrophages after LPS stimulation with or without d-RuO_2 nanozyme treatment for 24 h. (h) Representative images of immunofluorescence staining for Cox2, iNos, Tnf-α, and Il-1β in RAW264.7 macrophages after LPS stimulation

https://doi.org/10.1021/acsnano.5c04011
ACS Nano 2025, 19, 23080−23095

Figure 4. continued

with or without d-RuO_2 nanozyme treatment for 36 h. Scale bar, 50 μm. (i–l) Quantification of Cox2 (i), iNos (j), Tnf-α (k), and Il-1β (l), respectively. Data are shown as mean ± SD (n = 3) and analyzed using one-way ANOVA with Tukey's posthoc test. *P < 0.05; **P < 0.01; ***P < 0.001.

subsequently assessed the cell viability using a CCK-8 kit. We observed that d-RuO_2, at concentrations ranging from 0 μg/mL to 25 μg/mL, did not significantly affect the relative cell viability when compared to the control group (Figure S7). We then performed calcein-AM/PI staining on RAW264.7 macrophages cocultured with d-RuO_2 nanozyme at different concentrations. The results revealed no significant difference in the percentage of dead cells relative to the control group in the concentration ranging from 0 μg/mL–25 μg/mL (Figure S8). Based on the above results, a concentration of 25 μg/mL of d-RuO_2 nanozyme was selected for our subsequent experiments. We also stimulated RAW264.7 macrophages with 100 ng/mL lipopolysaccharide (LPS) and treated them with 25 μg/mL d-RuO_2 for 24 h before performing calcein-AM/PI staining. As shown in Figure S9, the d-RuO_2 could mitigate cell death induced by LPS. In *in vivo* assessment, H&E staining was performed on the hearts, livers, spleens, lungs, and kidneys, using the mice with and without undergoing knee joint injections of d-RuO_2 for 8 weeks. Histological analysis showed no notable differences in tissue morphology or inflammatory cell infiltration among the various groups (Figure S10), indicating that d-RuO_2 nanozyme exhibited no observable toxicity *in vivo*. Overall, d-RuO_2 nanozyme exhibited good biosafety both *in vitro* and *in vivo* within the appropriate concentration ranges.

To track the *in vivo* biodistribution and metabolic pathway of d-RuO_2, we labeled the d-RuO_2 with the near-infrared fluorescent dye Cy5. Successful labeling was confirmed by UV–vis spectroscopy, where a distinct absorption peak at ∼650 nm corresponded to the characteristic wavelength of Cy5 (Figure S11). Following intra-articular injection of d-RuO_2-Cy5 into knee joints, real-time fluorescence imaging revealed a pronounced fluorescence signal localized at the injection site immediately postadministration, which diminished completely within 6 h (Figure S12). To quantify systemic biodistribution, tissues (heart, liver, spleen, lungs, kidneys, joints) and excretions (urine, feces) were harvested at predetermined time points for ruthenium quantification. As shown in Figure S13, significant ruthenium accumulation was detected in the liver and fecal samples. These findings suggested a predominant hepatic metabolic pathway for d-RuO_2, with subsequent fecal elimination. Notably, urinary ruthenium remained undetectable throughout the study. This absence can be attributed to the diameter of d-RuO_2 (∼250 nm), which far exceeds the glomerular filtration size cutoff (∼5.5 nm).

Defective RuO_2 Nanozyme Suppresses LPS-Induced Macrophage Inflammation *In Vitro*. Macrophage accumulation in the synovial intimal lining of joints is a key morphological characteristic of synovitis, which significantly contributes to the progression of OA.[32,33] Given the previously reported antioxidant/anti-inflammatory effects of various nanozymes,[34] we investigated the anti-inflammatory effects of d-RuO_2 nanospheres using an *in vitro* macrophage inflammation model induced by LPS. LPS induces M1 macrophage polarization which exhibits pro-inflammatory properties and produces numerous inflammatory factors.[33,35] RAW264.7 macrophages were stimulated with LPS (100 ng/mL, 36 h), resulting in a marked increase in the protein expression levels of inducible nitric oxide synthase (iNos) and cyclooxygenase-2 (Cox2), which are well-established biomarkers of inflammatory macrophages,[36] compared to the control group (Figure 4a–c), corroborating the successful induction of inflammation in the macrophages. However, this trend was attenuated in the group of RAW264.7 macrophages cotreated with 100 ng/mL LPS and 25 μg/mL d-RuO_2 nanozyme for 24 h (Figure 4a–c). We found that the increased mRNA expression levels of *Inos*, prostaglandin-endoperoxide synthase 2 (*Ptgs2*), tumor necrosis factor (*Tnf*), and interleukin-1b (*Il1b*) observed in the LPS group were reversed when cotreated with d-RuO_2 (Figure 4d–g). Furthermore, the expression of inflammatory proteins on individual cells was examined by cell immunofluorescence. As displayed in Figure 4h–l, the increase of $Cox2^+$ and $iNos^+$ RAW264.7 macrophage percentage and an increasing trend in the fluorescence intensity of Tnf-α and Il-1β induced by LPS was observed. When treated with d-RuO_2 nanozyme, these rising trends were reversed. Taken together, d-RuO_2 nanozyme effectively suppressed the LPS-induced macrophage inflammation *in vitro*, indicating their appreciable anti-inflammatory properties.

Defective RuO_2 Nanozyme Improves Behavioral Performance in Mice. Pain of joint and impaired mobility are common symptoms of OA. To evaluate the therapeutic efficacy of d-RuO_2 nanozyme *in vivo*, a series of behavioral tests were conducted to investigate the pain and functional improvement of mice knees after 8 weeks of treatment (Figure 5a). First, we analyzed gait changes in mice using footprint experiments. In the sham group, the front and rear footprints of the mice were relatively overlapping, similar to the walking habits of normal mice. When the mice had pain and impaired mobility in their limbs, those footprints were significantly separated, as shown by the footprints in the DMM group. As shown in the first image of Figure 5b, we defined several measurement parameters related to the footprints of mice: the distance between the neighboring front and rear footprints on the same side of mice as the front/rear print length; the distance between two neighboring footprints of the same paw as the stride length; while the distance between neighboring front or rear footprints on different sides as the step length. The results showed that the d-RuO_2 nanozyme treatment reduced the relative front/rear print length, and increased the relative step length and stride length in the DMM mice (Figure 5b–e), indicating an improvement in pain and joint condition.

To assess the pain status of the knee joint in mice, the von Frey Fiber test was performed and we found that the pain threshold of DMM mice treated with knee injection of d-RuO_2 nanozyme was significantly higher than that of the untreated DMM group (Figure 5f), indicating an increased pain tolerance in the treated mice. Meanwhile, we allowed the mice to move spontaneously in a 50 cm × 50 cm open field for 3 min and recorded their activity data. Our findings showed that the mice undergoing DMM surgery exhibited reduced relative activity, distance, and mean speed compared to the sham group. Surprisingly, their poor motility was significantly

https://doi.org/10.1021/acsnano.5c04011
ACS Nano 2025, 19, 23080–23095

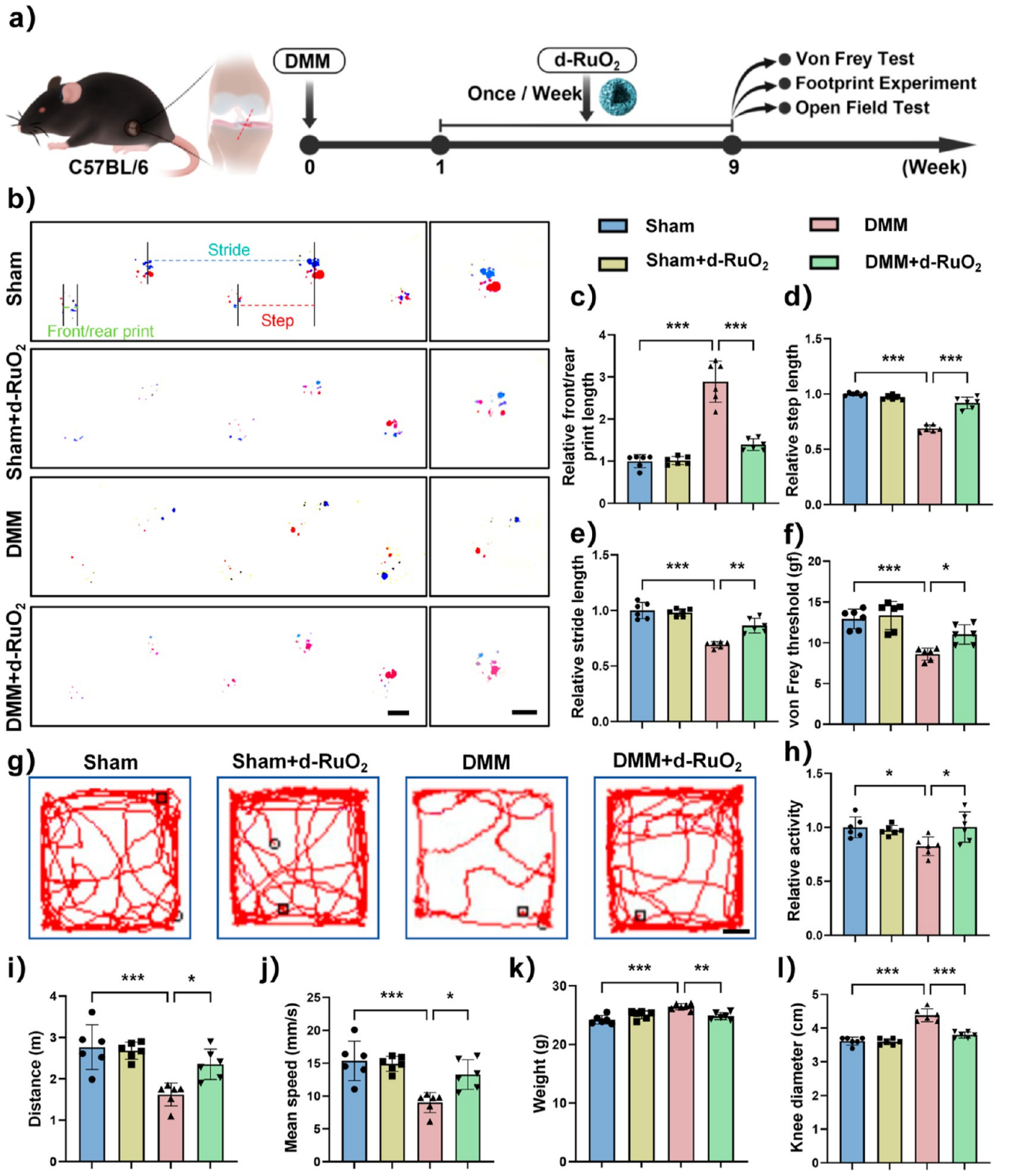

Figure 5. Defective RuO_2 nanozyme improves behavioral performance in DMM mice. (a) Timeline of the animal experiments. (b) Representative images of the footprints of each group. Scale bars, 1 cm. (c–e) Quantification of mice footprints including relative front/rear print length (c), relative step length (d), and relative stride length (e). (f) Quantification of thresholds of paw contraction to mechanical stimulation by von Frey test. (g) Representative trajectories of mice in open field test. Squares and circles indicate the start and end points of the mice's locomotion, respectively. Scale bar, 10 cm. (h–j) Quantification of relative activity (h), distance (i), and mean speed (j) of mice in the open field test. (k,l) Weight (k) and knee diameter (l) of mice treated as indicated. Data are shown as mean ± SD ($n = 6$) and analyzed using one-way ANOVA with Tukey's posthoc test. *$P < 0.05$; **$P < 0.01$; ***$P < 0.001$.

improved with d-RuO_2 treatment (Figure 5g–j). In addition, both the body weight and knee diameter of the mice were measured, and we observed a significant increase in the DMM surgery group compared to the sham surgery group. Swollen knees and increased weight in DMM mice were alleviated following the treatment of d-RuO_2 (Figure 5k,l). We

https://doi.org/10.1021/acsnano.5c04011
ACS Nano 2025, 19, 23080–23095

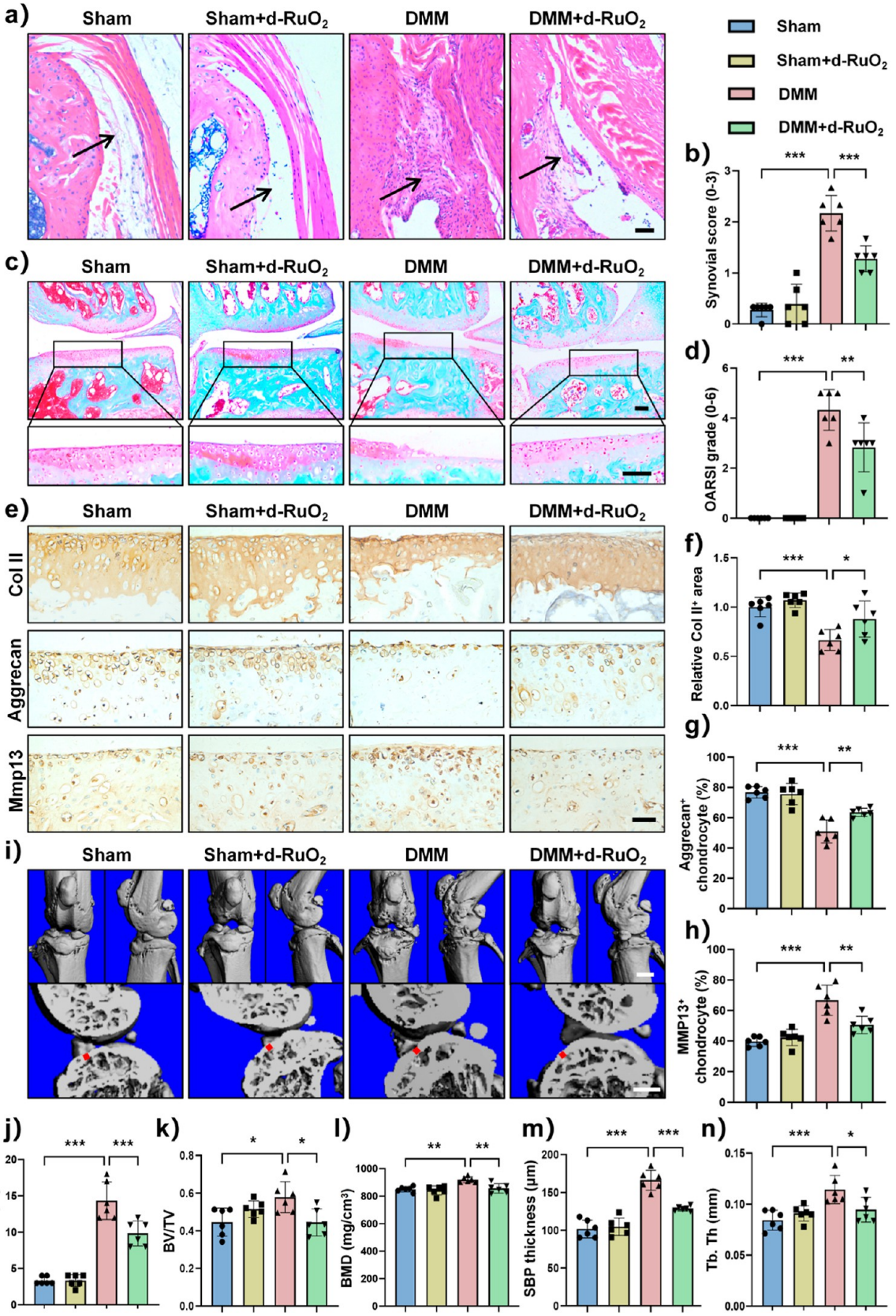

Figure 6. Defective RuO_2 nanozyme attenuates synovitis, cartilage degeneration and abnormal bone remodeling in DMM mice. (a) Representative images of H&E staining of the mouse knee joints. Arrows indicate synovium of the mouse knee joints. Scale bar, 25 μm. (b) Quantification of the synovial score in (a). (c) Representative images of safranin-O/fast green staining of the mouse knee joints. Scale bars, 100 μm. (d) Quantification of the OARSI grade in (c). (e) Representative images of IHC staining for Col II, Aggrecan, and Mmp13 in the articular cartilage of mice. Scale bars, 20 μm. (f–h) Quantification of IHC staining of Col II (f), Aggrecan (g), and Mmp13 (h) in the articular cartilage. (i) Representative images of Micro-CT three-dimensional reconstruction of the mouse knee joints. Scale bars, 1 mm

https://doi.org/10.1021/acsnano.5c04011
ACS Nano 2025, 19, 23080–23095

Figure 6. continued

(upper panel), 0.5 mm (lower panel). (j−n) Quantitative analysis of the number of osteophytes (j), the ratio of subchondral bone volume to tissue volume (BV/TV) (k), subchondral bone mineral density (BMD) (l), SBP thickness (m), and trabecular thickness (Tb. Th) (n) in the knee joints of mice. Data are shown as mean ± SD (n = 6) and analyzed using one-way ANOVA with Tukey's posthoc test (f−h, j−n) or the Kruska−Wallis test (b,d). *P < 0.05; **P < 0.01; ***P < 0.001.

hypothesized that the increased pain and poor joint condition in DMM mice resulted in reduced physical activity, which subsequently led to calorie accumulation and weight gain.[37] Thus, the above data suggest that d-RuO_2 nanozyme can alleviate knee pain and improve locomotor activity in DMM mice.

Defective RuO_2 Nanozyme Alleviates KOA Progression. Synovitis, cartilage degeneration, and abnormal bone remodeling are typical pathological features of OA.[3,38] To investigate the effect of d-RuO_2 on the pathological progression of OA, histological analysis of the knee joints in mice was performed. First, knee synovitis was assessed using H&E staining; we noticed lesser inflammatory cell infiltration, mitigated synovial hyperplasia, and lower synovitis scores in the treatment group than in the DMM one (Figure 6a,b), suggesting d-RuO_2 could alleviate knee synovitis. Next, knee cartilage degeneration was evaluated by staining with safranin-O/fast green and toluidine blue. From the stained images, the knee articular cartilage in the DMM group exhibited degenerative changes, including surface fibrillation, thinning, and even loss of articular cartilage (Figures 6c and S14a). Surprisingly, when compared to the DMM group, DMM mice treated with d-RuO_2 had a lower OARSI score (Figure 6d), and thicker uncalcified cartilage thickness (Figure S14b), indicating reduced cartilage degeneration. Furthermore, immunohistochemical staining revealed that the expression of cartilage catabolic metabolism marker (MMP13) was also reduced and anabolic metabolism markers (Col II and Aggrecan) were elevated in the treatment group relative to the DMM group (Figure 6e−h). The above findings suggested that d-RuO_2 promotes chondrocyte anabolism while reducing catabolism, thereby slowing down cartilage degeneration.

Osteophytes and changes in subchondral bone, including sclerosis, capsulitis, and marrow edema, are characteristic of abnormal bone remodeling that occurs during the progression of OA pathogenesis.[38] To further evaluate the effect of nanozyme on abnormal bone remodeling during OA pathology, Micro-CT scans as well as three-dimensional reconstructions were performed on the mouse knee joints (Figure 6i). By analyzing the CT data, we observed anomalous bone remodeling in the joints of the DMM group. The remodeling included roughening of the articular surfaces, narrowing of the joint space, formation of fatty bone, and sclerosis of the subchondral bone (Figure 6i). These changes were quantified by measuring several parameters: increased knee bone volume (BV) (Figure S14c), the number of osteophytes, the ratio of subchondral bone volume to tissue volume (BV/TV), bone mineral density (BMD), subchondral bone plate (SBP) thickness, and trabecular thickness (Tb.Th) (Figure 6j−n). However, these pathological alterations were remarkably reversed after treatment with d-RuO_2, substantiating the efficacy of d-RuO_2 in the improvement of bone remodeling during OA pathology. Our observations demonstrated that d-RuO_2 nanozyme significantly alleviated the pathological progression of KOA, including relieving synovitis, delaying articular cartilage damage, and reducing abnormal bone remodeling, such as osteophyte formation and subchondral osteosclerosis.

Defective RuO_2 Nanozyme Alleviates Oxidative Stress by Inhibiting the ROS/NLRP3/Caspase-1 Signaling Pathway. To further explore the potential mechanism by which d-RuO_2 nanozyme alleviates OA, we assessed their ability to scavenge ROS. Intracellular ROS levels in RAW264.7 macrophages were measured using a DCFH-DA assay kit after 24 h of LPS stimulation, with or without treatment with d-RuO_2 nanozyme. The results indicated that d-RuO_2 significantly diminished the LPS-induced elevation in ROS levels (Figure 7a,b), indicating their potent ROS scavenging ability. Oxidative stress is caused by an imbalance between the production and elimination of ROS in the cell; with increased ROS quenching, oxidative stress is alleviated accordingly.[9]

The NLRP3 inflammasome, consisting of the sensor NLRP3, the bipartite adaptor ASC, and the effector enzyme pro-caspase-1,[12] plays an important role in various diseases related to microbial and sterile inflammation, including autoinflammatory disorders and resisting host immune defenses against bacterial, fungal, and viral infections.[39−42] ROS serve as activators that promote the assembly of the NLRP3 inflammasome, leading to the recruitment of macrophages and neutrophils, which in turn results in the production of more ROS, exacerbating inflammation and creating a feedback loop.[12] More specifically, upon activation, NLRP3 oligomerizes interact with ASC, which promotes the recruitment of pro-caspase-1 to NLRP3 inflammasome, leading to the assembly of NLRP3 inflammasome.[43,44] Following this, pro-caspase-1 is activated into cleaved-caspase-1 and promotes the maturation of the pro-inflammatory cytokines, further enhancing the inflammatory response.[13,45,46] Given their crucial roles, we examined the expression of key proteins in the ROS/NLRP3/Caspase-1 signaling pathway in RAW264.7 macrophages after LPS stimulation, with or without d-RuO_2 nanozyme treatment, by immunofluorescence staining (Figure 7c) and Western blot (Figure 7d). We found that the increased expression levels of Nlrp3, Pro-caspase-1, Cleaved-caspase-1, and Asc, after being stimulated by LPS, were reversed by treatment with nanozyme (Figure 7c,d,f−l). Next, we performed tissue immunofluorescence staining to macrophage markers (F4/80) costained with Nlrp3, Caspase-1, and Asc in the mouse knee synovium.[47] Nnrp3, Caspase-1, and Asc colocalized with macrophages ($F4/80^+$) were markedly increased in the DMM group compared to the sham group. However, the observed trends were notably reduced in the treatment group (Figure 7e,m−o). These results implied that d-RuO_2 nanozyme attenuated LPS-induced priming and activation of the ROS/NLRP3/Caspase-1 signaling pathway.

CONCLUSIONS

We presented defective RuO_2 nanospheres as a ROS scavenger to attenuate OA progression. It was shown that compared to the crystalline RuO_2, the d-RuO_2 hollow nanospheres exhibited greater antioxidant capacity; cellular experiments revealed that d-RuO_2 reduced the expression of the biomarkers of

https://doi.org/10.1021/acsnano.5c04011
ACS Nano 2025, 19, 23080−23095

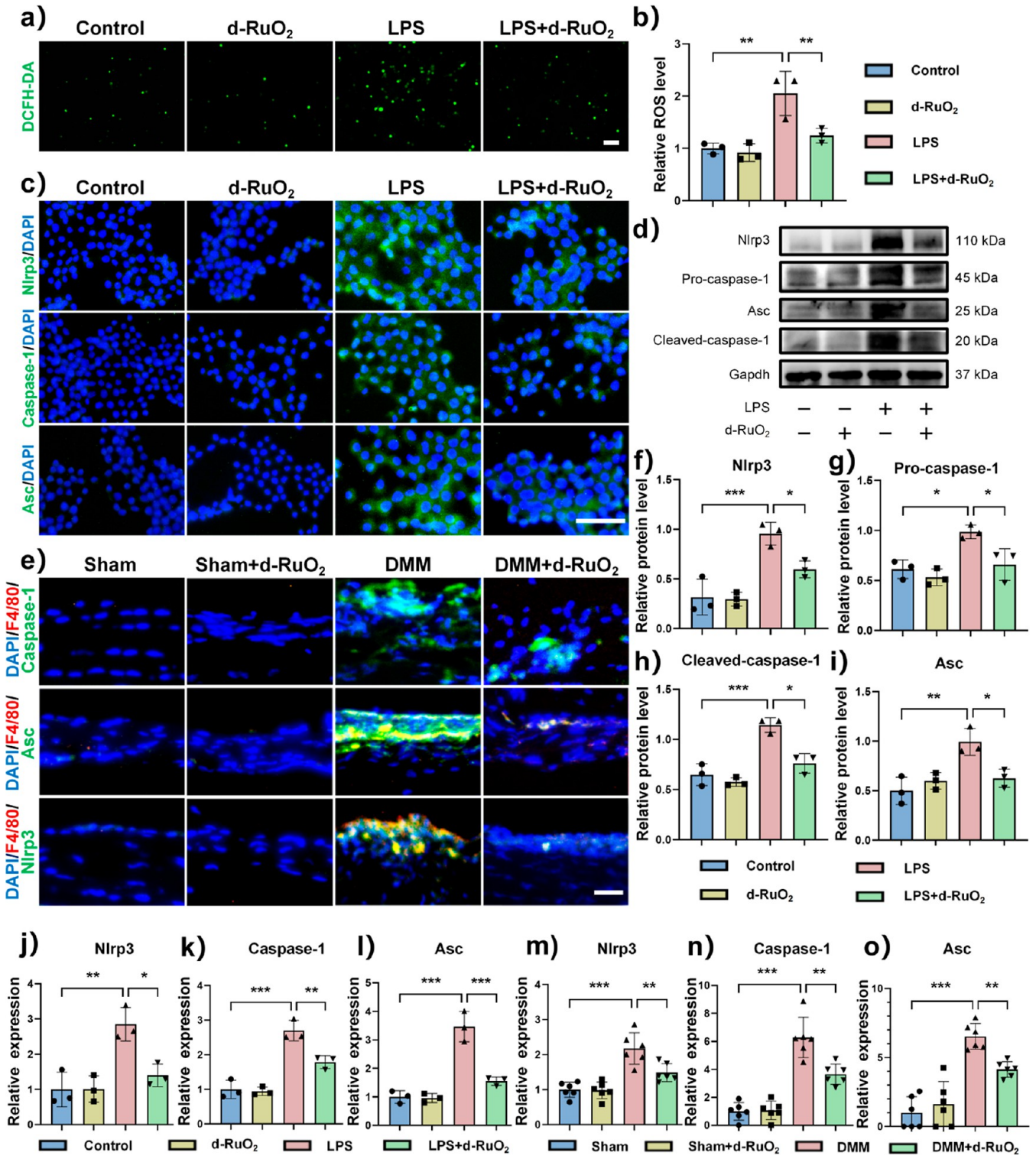

Figure 7. Defective RuO_2 nanozyme inhibits the ROS/NLRP3/Caspase-1 signaling pathway. (a) Representative images of ROS detection in RAW264.7 macrophages after LPS stimulation with or without d-RuO_2 nanozyme treatment for 24 h. Scale bar, 100 μm. (b) Quantification of the ROS levels in (a). Data are shown as mean ± SD (n = 3) and analyzed using one-way ANOVA with Tukey's posthoc test. **P < 0.01. (c) Representative images of immunofluorescence staining for Nlrp3, Caspase-1, and Asc in RAW264.7 macrophages after LPS stimulation with or without d-RuO_2 nanozyme treatment for 36 h. Scale bar, 50 μm. (d) Representative Western blot images of Nlrp3, Pro-caspase-1, Cleaved-caspase-1, and Asc expression in RAW264.7 macrophages after LPS stimulation with or without d-RuO_2 nanozyme treatment for 36 h. (e) Representative images of F4/80 coimmunofluorescence with Nlrp3, Caspase-1, and Asc in the synovium of mouse knee joints by sham or DMM surgery treated as indicated. Scale bar, 25 μm. (f–i) Quantification of relative protein expression of Nlrp3 (f), Pro-caspase-1 (g), Cleaved-caspase-1 (h), and Asc (i) in (d). Data are shown as mean ± SD (n = 3) and analyzed using one-way ANOVA with Tukey's posthoc test. *P < 0.05; **P < 0.01; ***P < 0.001. (j–l) Quantification of relative expression levels of Nlrp3 (j), Caspase-1 (k), and Asc (l) in immunofluorescence staining of cells in (c). Data are shown as mean ± SD (n = 3) and analyzed using one-way ANOVA with Tukey's posthoc test. *P < 0.05; **P < 0.01; ***P < 0.001. (m–o) Quantification of relative expression levels of Nlrp3 (m), Caspase-1 (n), and Asc

https://doi.org/10.1021/acsnano.5c04011
ACS Nano 2025, 19, 23080–23095

Figure 7. continued

(o) in immunofluorescence staining of tissues in (e). Data are shown as mean ± SD (n = 6) and analyzed using one-way ANOVA with Tukey's posthoc test. **P < 0.01; ***P < 0.001.

inflammatory macrophages and eliminated the ROS to alleviate oxidative stress. Significant improvements in pain and physical activity, along with the alleviation of synovitis, cartilage degeneration, and abnormal bone remodeling in the DMM mice were observed following the treatment with d-RuO_2. Additionally, the mechanistic study revealed that d-RuO_2 reduced the expression levels of NLRP3, a key protein in the process of inflammation, implying that d-RuO_2 delayed the progression of OA via suppressing the ROS/NLRP3/Caspase-1 signaling pathway. This study provides a potential therapeutic strategy for OA.

MATERIALS AND METHODS

Materials. Hydrous ruthenium chloride ($RuCl_3{\cdot}xH_2O$), ethylene glycol (EG), copper nitrate trihydrate ($Cu(NO_3)_2{\cdot}3H_2O$), polyvinylpyrrolidone (PVP, MW ∼ 40,000), ammonium hydroxide (25% NH_4OH), and sodium hydroxide (NaOH) were obtained from Aladdin Chemical Co. Ltd. (Shanghai, China). The SOD assay kit was purchased from Dojindo Laboratories, Japan. Hydroxyl radical quenching measurement was carried out using a kit obtained from Nanjing Jiancheng Bioengineering Institute. All the other reagents and chemicals were bought from commercial sources and used as received. Deionized water (18.2 MΩ·cm, Millipore) and absolute ethanol were used during all the experiments.

Characterizations. The material characterization was conducted using various analytical techniques. A scanning electron microscope (Ultra 55, Zeiss, Germany) and transmission electron microscopes (FEI TECNAI G2 F20 and JEOL JEM-2100F, 200 kV) provided the structural and morphological information. The aberration-corrected high-angle annular dark-field scanning transmission electron microscope (HAADF-STEM) images were collected by a FEI Themis Z device (Thermo Fisher Scientific), and the accelerating voltage was 300 kV. The elemental compositions were evaluated using an inductively coupled plasma optical emission spectrometer (Avio 220 Max, PerkinElmer). The powder XRD patterns were obtained using a diffractometer (Rigaku Ultima III, Japan) with Cu Kα radiation. X-ray photoelectron spectroscopic (XPS) studies were carried out on a Thermo Scientific K-Alpha spectrometer (Al Kα (1486 eV)) having a hemispherical energy analyzer (C 1s calibrated the binding energy at 284.8 eV). UV−visible absorption analysis was performed on a microplate reader (SpectraMax M2e, Molecular Devices Co. Ltd., Shanghai, China). The catalase-like activity was assessed through a dissolved oxygen meter (SevenExcellence Multiparameter, Mettler Toledo Co. Ltd.) presented in milligrams per liter. A Thermo Scientific Nicolet iS 5 FTIR Spectrometer (USA) was employed for FTIR analysis. Raman characterization was done using a Renishaw inVia Raman microscope with a 633 nm laser. Thermogravimetric analysis (TGA) was carried out using a Mettler Toledo TGA-2 with a heating rate of 10 °C/min under air.

Synthesis of d-RuO_2 Nanospheres. Cuprous oxide (Cu_2O) was used as a nanotemplate to synthesize d-RuO_2 nanospheres. Following our previously reported method, 300 mg of PVP and 480 mg of $Cu(NO_3)_2{\cdot}3H_2O$ were first dissolved in 50 mL of water-free EG.[30] The transparent solution was heated to 185 °C in an oil bath while being vigorously stirred. This temperature was maintained for 60 min to obtain the orange-colored Cu_2O. The product was separated by centrifugation (10,000 rpm, 30 min) and washed with ethanol and distilled water twice. To grow hydrous d-RuO_2 onto the surface of Cu_2O, the nanospheres were exposed to an aqueous solution of $RuCl_3$: the water-dispersed Cu_2O (100 mg, 5 mg/mL) was treated with an aqueous solution of $RuCl_3{\cdot}xH_2O$ (150 mg, 2 mL) under vigorous stirring (30 min) at room temperature. Later, the solution was centrifuged to remove any unreacted or released salts. In the next step, the obtained Cu_2O@d-RuO_2 core−shell nanostructure was redispersed in 20 mL of water and the pH of the solution was tuned to 10 along with the addition of 100 μL of (30%) H_2O_2 under stirring. To improve the quality of the d-RuO_2, the solution was also heated at 80 °C for 30 min and the Cu_2O@d-RuO_2 product was recovered via centrifugation and washed with water. In the final step, the undesired Cu_2O core was completely etched using NH_4OH (25%): the Cu_2O@d-RuO_2 nanospheres (30 mg) were dispersed in 5 mL of deionized water and then 1 mL of 25% NH_4OH was slowly added under stirring. After 1 h of incubation in an ammonia solution, the final PVP-capped hollow-structured d-RuO_2 nanospheres were collected and washed with water and ethanol.

Superoxide Dismutase-like Activity Measurements. The SOD-like activity of d-RuO_2 and thermally treated RuO_2 was evaluated using a WST-1 assay kit. The RuO_2 samples with a specific concentration were combined with 200 μL of the working solution in a microplate well. Then, 20 μL of the enzyme working solution was added, and the mixture was incubated for 20 min at 37 °C. The absorbance (450 nm) was evaluated by a multiple plate reader. The amount of superoxide radical scavenging was calculated by measuring the inhibition in formazan color development. The analysis was performed in triplicate (n = 3).

Catalase-like Activity Measurements. We evaluated the CAT-like activity of d-RuO_2 and thermally treated RuO_2 by monitoring the amount of catalytically generated dissolved oxygen with an oxygen meter. The RuO_2 samples with a concentration of 1 μg/mL were added to 6 mL of water. The concentration of H_2O_2 during the testing was kept at 5 mM, and the amount of nanozyme-triggered generation of oxygen (milligram per liter) was monitored for 10 min.

Hydroxyl Radicals Scavenging Measurements. The capacity of hydroxyl radicals ($^{\bullet}OH$) scavenging was determined using the $^{\bullet}OH$-assay kit. Following the instructions of the kit, different concentrations (6.25, 12.5, 25, 50, and 100 μg/mL) of both d-RuO_2 and thermally treated RuO_2 were mixed with the preprepared reagent solution and chromogenic agent, followed by a 20 min incubation at room temperature. The absorbance (550 nm) was then measured using a microplate reader to quantify the amount of hydroxyl radicals. The detection of $^{\bullet}OH$ was based on the classical Fenton reaction principle, where the Griess reagent was used for the visualization of hydroxyl radical production. To guarantee the accuracy, the analysis was performed in triplicate (n = 3).

Cell Culture. RAW264.7 macrophages and SW982 cells were purchased from the Chinese Academy of Science's Cell Bank of Type Culture Collection (Shanghai, China). The mouse primary chondrocytes were collected from the ribs of 3 day-old C57BL/6 mice. RAW264.7 macrophages were cultured in Dulbecco's modified Eagle's medium (DMEM, Gibco) containing 10% fetal bovine serum (FBS, Gibco), 1% penicillin and streptomycin (Gibco) at 37 °C and 5% CO_2. SW982 cells and chondrocytes were cultured in DMEM/F12-Dulbecco's modified Eagle's medium (Gibco) with 10% FBS and 1% penicillin and streptomycin at 37 °C and 5% CO_2. Macrophages were stimulated into an inflammatory state using 100 ng/mL lipopolysaccharide (LPS, #L2630, Sigma-Aldrich, St. Louis, MO, USA).

Cell Counting Kit-8 (CCK8) Assay. RAW264.7 macrophages, SW982 cells, and chondrocytes were seeded into 96-well cell culture plates and cultured until the cell density reached 80%, then d-RuO_2 nanozyme was added at different concentrations (0, 1, 5, 10, 25, 50, and 100 μg/mL). Cell activity was evaluated using a CCK-8 assay kit (Dojindo, Japan) after 24 h. After washed by phosphate-buffered saline (PBS), 100 μL 10% CCK-8 solution was added to each well and incubated for 1 h at 37 °C in a temperature chamber (Senxin,

https://doi.org/10.1021/acsnano.5c04011
ACS Nano 2025, 19, 23080−23095

China). Then the optical density value was measured at 450 nm using a spectrophotometer (Thermo Scientific, USA).

Calcein-AM/PI Double Staining. RAW264.7 macrophages were seeded into 24-well cell culture plates and cultured until the cell density reached 50%, then d-RuO_2 nanozyme was added to the culture medium at different concentrations (0, 1, 5, 10, 25, 50, 75, and 100 μg/mL). After 24 h of incubation, cells were stained for live and dead cells using a calcein AM/PI Cell staining kit (Beyotime, China) according to the manufacturer's instructions. Then the staining of the cells was observed using a fluorescence microscope (Zeiss, Germany) to count the number of live and dead cells.

Measurement of Intracellular ROS Levels. When the density of RAW264.7 macrophages seeded in 24-well plates reached 50%, LPS and d-RuO_2 were added according to the grouping. Twelve hours later, intracellular ROS levels were detected using a DCFH-DA assay kit (Beyotime, China) at 37 °C for 30 min. Fluorescence images were then obtained using a fluorescence microscope (Zeiss, Germany), and the fluorescence intensity was measured by ImageJ software (version 1.8.0, USA).

Quantitative Real Time-PCR (qPCR). All cellular mRNA from RAW264.7 macrophages was extracted using the RNA quick Purification Kit (ES Science, China) and then reverse transcribed to obtain cDNA using reverse transcription reagents (Vazyme, China) according to the instructions. The qPCR analysis was performed using the ChamQ Universal SYBR qPCR Master Mix (Vazyme, China) on a Light Cycler 480 PCR System (Roche, Switzerland). The primer sequences used are listed in Table S1.

Western Blot. Total cellular proteins of RAW264.7 macrophages were extracted using RIPA Lysis Buffer (Solarbio, China) containing protease and phosphatase inhibitor cocktail (Solarbio, China) for 15 min at 4 °C. Protein concentration was determined using a Quick Start Bradford 1× Dye Reagent (Bio-Rad, USA) after protein lysates were centrifuged at 1500 rpm for 15 min at 4 °C. Proteins were separated using SDS-PAGE (Epizyme, China) and then transferred to a PVDF membrane (Sigma-Aldrich, USA). Then the membrane was immersed in a 5% milk (Biofroxx, Germany) solution for 1 h. After washed three times with Tris-buffered saline/Tween (TBST), the membrane was incubated with 1:1000 primary antibodies for 8 h at 4 °C. The membrane was then incubated with a 1:10,000 dilution of secondary antibodies, HRP-anti-IgG (Biosharp, China) for 1 h at room temperature after washed by TBST. The ChemiDocXRS and Imaging System (Tanon, China) was used to detect all images. Finally, proteins were analyzed quantitatively using ImageJ software (version 1.8.0, USA).

Animal Study. The experimental animals were 12 week-old male C57BL/6 mice (22−24 g) purchased from Gempharmatech (Nanjing, China). All mice were fed in a specific pathogen-free (SPF) environment with free access to food and water. The mice underwent a destabilization of the medial meniscus (DMM) surgery on the right knee to induce the KOA model. Intra-articular injections into the right knee joints were initiated one-week postsurgery and performed weekly for 8 weeks. Then mice were harvested, and specimens of hearts, livers, spleens, lungs, kidneys, and knee joints were collected. The animal protocols were approved by the Use Committee of Nanjing Drum Tower Hospital, Nanjing University Medical School (2024AE01035).

The mice were randomly divided into four groups: (1) Sham surgery; (2) Sham surgery with d-RuO_2 treatment (25 μg/mL, 8 μL, once a week); (3) DMM surgery; (4) DMM surgery with d-RuO_2 treatment (25 μg/mL, 8 μL, once a week). The mice in the sham surgery and DMM surgery groups were injected with normal saline at the same dose and frequency as the treatment groups.

DMM-Induced KOA Model. Inhalation anesthesia was administrated using isoflurane in 12 week-old C57BL/6 male mice, and then the right knee joint was prepared and disinfected routinely. A medial parapatellar incision was made, followed by blunt dissection of the fat pad to expose the medial meniscotibial ligament (MMTL) under a stereoscopic microscope. The MMTL between the anterior horn of the medial meniscus and the intercondylar ridge of the tibial plateau was cut, resulting in complete destabilization of the medial meniscus. The operation of the sham group was the same as that of the DMM group except that the MMTL was not cut.

Footprint Experiment. Mice were marked with red ink on their front paws and blue ink on their hind paws, then placed on a white paper-lined track (70 cm × 20 cm) to walk freely, leaving ink blots that recorded their trajectories. Each mouse completed the test three times. Relative step length, stride length, and front/rear print length were measured to evaluate their activity levels and pain during natural walking. This experiment was conducted in a relatively dark and quiet environment, and the mice were acclimatized in this environment for 1 week before the experiment.

Open Field Test (OFT). Mice were placed in an open field (50 cm × 50 cm) and allowed to move freely for 3 min. Their spontaneous activity trajectories were recorded using a tracking system equipped with an infrared camera (Zhenghua Technology, China). Relative activity, total distance traveled, and mean speed were analyzed to evaluate their spontaneous activity and exploratory behavior. The experiment was performed in a quiet, dark environment to minimize external disturbances.

von Frey Fiber Test. Mechanical pain sensitivity in mice was assessed using an electronic von Frey device (IITC, Woodland Hills, USA). Mice were placed in a cage (4 cm × 3 cm × 7 cm) with a metal mesh bottom, and the von Frey fiber was applied to the plantar surface of the mouse's right hind paw foot from the bottom of the cage, gradually increasing the force until the mouse retracted its right hind foot, at which point the threshold of the peak detector was recorded. The numerical magnitude of the threshold was negatively correlated with pain sensitivity in mice.

Microcomputed Tomography (Micro-CT) Analysis. Mouse knee joints were evaluated by a Micro-CT scanner (VivaCT80, Scanco Medical AG, Switzerland) at 70 kV, 114 μA. Three-dimensional images of knee joints were reconstructed using Scanco Medical software (Scanco threshold: 220). We analyzed the cancellous bone and 3D-reconstructed images to quantify parameters related to osteophytes, trabeculae, and subchondral bone using Scanco Medical software.

Histological Analysis. After Micro-CT scanning, mouse knee joints were immersed in 10% EDTA solution (Biofroxx, Germany) for decalcification. After paraffin embedding of the knee joints, the tissues were sliced into 5 mm thick sections using a microtome (Thermo, Germany). Then we assessed synovitis as well as cartilage degeneration in the knee joint by the synovitis score (0−3) and Osteoarthritis Research Society International (OARSI) scoring system (0−6) after hematoxylin and eosin (H&E) (#C0105S, Beyotime), Safranin-O/fast green (S.O.) (#G1371, Solarbio) and Toluidine Blue (#G2543, Solarbio) staining.

Immunohistochemical Staining. Mouse knee joint slides were soaked in 3% H_2O_2 for 15 min to inactivate endogenous oxidase after being dewaxed and hydrated in xylene and graded alcohol. After 3 washes by PBS, the slides were treated with 0.2% pepsin (Sigma-Aldrich, USA) for antigen repair for 1 h at 37 °C. Then the slides were blocked with 5% bovine serum albumin (BSA) for 1 h and then incubated with 1:200 primary antibodies for 8 h at 4 °C. After being washed with TBST 3 times, the slides were incubated with 1:10,000 secondary antibodies of HRP-anti-IgG (Biosharp, China) for 1 h at room temperature. Color development was then performed using a DAB Kit (Typing, China). The nucleus was stained with hematoxylin and then sealed with resin.

Immunofluorescence Staining. In tissue immunofluorescence experiments, mouse knee joint slides were incubated with 0.2% pepsin for 1 h at 37 °C after dewaxing and hydration. After 3 washes with PBS, slides were blocked with 5% BSA for 1 h and then incubated with 1:200 primary antibodies for 8 h at 4 °C. The sections were rewarmed and washed 3 times with TBST and then incubated with 1:200 fluorescein isothiocyanate (FITC)-coupled secondary antibody at 37 °C for 1 h. The nucleus was stained with 2-(4-amidinophenyl)−6-indolecarbamidine dihydrochloride (DAPI). The sections were sealed and observed under a fluorescence microscope (Zeiss, Germany). In immunofluorescence experiments of RAW264.7 macrophages, after being fixed with 4% paraformaldehyde for 15

https://doi.org/10.1021/acsnano.5c04011
ACS Nano 2025, 19, 23080−23095

min, 0.1% Triton-X-100 was used to perforate the cell membrane for 15 min. The next steps are the same as the immunofluorescence steps for tissues above.

Biodistribution and Metabolism. Eight-week-old C57BL/6 mice were anesthetized and administered a 50 μL intra-articular injection of d-RuO_2-Cy5 into the right knee joint. At 0, 6, 12, and 24 h postinjection, Cy5 fluorescence signals (Ex/Em: 640/670 nm) were acquired using a small animal *in vivo* imaging system (PerkinElmer IVIS) to analyze local retention in the knee joint and systemic biodistribution. Fecal and urine samples were collected at designated time intervals. Following imaging, mice were sacrificed and major organs (heart, liver, spleen, lungs, kidneys) along with joint tissues were harvested. All biological samples (excreta and tissues) were subjected to microwave-assisted digestion with aqua regia (200 °C, 30 min) for subsequent quantification of ruthenium content by inductively coupled plasma optical emission spectrometry (ICP-OES).

Antibodies. The primary antibodies used in this study included: rabbit anti-Gapdh (#8884, Cell Signaling Technology, USA); rabbit anti-Cox2 (#12282, Cell Signaling Technology, USA); rabbit anti-iNos (#13120, Cell Signaling Technology, USA); rabbit anti-Nlrp3 (#13158, Cell Signaling Technology, USA); rabbit anti-Caspase-1 (#22915-1-AP, Proteintech, China); rabbit anti-Asc (#10500-1-AP, Proteintech, China); rabbit anti-Col II (#BA0533, Boster, China), rabbit anti-Aggrecan (#A12045, ABclonal Biotechnology, China); rabbit anti-Mmp13 (#18165-1-AP, Proteintech, China); mouse anti-F4/80 (#sc-377009, Santa Cruz, CA, USA).

Statistical Analysis. Quantitative data represents at least three independent experiments. All data processing and statistical analysis were performed using GraphPad Prism software (version 9.5). The data were subjected to the Shapiro–Wilk normality test and Levene's homogeneity of variance test. A paired two-tailed Student's *t*-test was used to compare the mean values between the two groups, and for more than two groups, one-way ANOVA followed by Tukey's posthoc tests was used. A Kruska Wallis test was used for the comparison of the OARSI score and synovitis score. Data were presented as mean values ± SD. $P < 0.05$ was considered statistically significant ($^*P < 0.05$, $^{**}P < 0.01$, $^{***}P < 0.001$), and ns represents no significance.

ASSOCIATED CONTENT

Supporting Information

The Supporting Information is available free of charge at https://pubs.acs.org/doi/10.1021/acsnano.5c04011.

Primer sequences of genes; SEM and TEM images of different nanostructures; XPS spectra and Raman spectra of defective and thermally treated RuO_2 nanospheres; relative cell viability of different cells; representative calcein-AM/PI staining of RAW264.7 macrophages; representative H&E staining of mouse organs; UV–visible spectral analysis of d-RuO_2-Cy5; near-infrared images of d-RuO_2-Cy5 *in vivo*; statistics of ruthenium content in organs and feces; representative images of toluidine blue staining of the mouse knee joints, and quantitative analysis of uncalcified cartilage thickness and BV (PDF)

AUTHOR INFORMATION

Corresponding Authors

Hui Wei − *Department of Biomedical Engineering, College of Engineering and Applied Sciences, Nanjing National Laboratory of Microstructures, Jiangsu Key Laboratory of Artificial Functional Materials, Nanjing University, Nanjing, Jiangsu 210023, PR China;* orcid.org/0000-0003-0870-7142; Email: weihui@nju.edu.cn

Ziying Sun − *Department of Orthopedics, Nanjing Jinling Hospital, Affiliated Hospital of Medical School, Nanjing University, Nanjing, Jiangsu 210002, PR China;* Email: ziyingsun@foxmail.com

Dongquan Shi − *Division of Sports Medicine and Adult Reconstructive Surgery, Department of Orthopedic Surgery, Nanjing Drum Tower Hospital, Affiliated Hospital of Medical School, Nanjing University, Nanjing, Jiangsu 210008, PR China; State Key Laboratory of Pharmaceutical Biotechnology, Nanjing University, Nanjing, Jiangsu 210023, PR China; Branch of National Clinical Research Center for Orthopedics, Sports Medicine and Rehabilitation, Nanjing, Jiangsu 210008, PR China;* orcid.org/0000-0002-4769-7816; Email: shidongquan@nju.edu.cn

Authors

Jie Lv − *Division of Sports Medicine and Adult Reconstructive Surgery, Department of Orthopedic Surgery, Nanjing Drum Tower Hospital, Affiliated Hospital of Medical School, Nanjing University, Nanjing, Jiangsu 210008, PR China; State Key Laboratory of Pharmaceutical Biotechnology, Nanjing University, Nanjing, Jiangsu 210023, PR China; Branch of National Clinical Research Center for Orthopedics, Sports Medicine and Rehabilitation, Nanjing, Jiangsu 210008, PR China*

Faheem Muhammad − *Department of Biomedical Engineering, College of Engineering and Applied Sciences, Nanjing National Laboratory of Microstructures, Jiangsu Key Laboratory of Artificial Functional Materials, Nanjing University, Nanjing, Jiangsu 210023, PR China; Guangdong Key Laboratory of Biomedical Measurements and Ultrasound Imaging, School of Biomedical Engineering, Shenzhen University Medical School, Shenzhen University, Shenzhen, Guangdong 518060, PR China*

Zheng Wang − *Division of Sports Medicine and Adult Reconstructive Surgery, Department of Orthopedic Surgery, Nanjing Drum Tower Hospital, Affiliated Hospital of Medical School, Nanjing University, Nanjing, Jiangsu 210008, PR China; State Key Laboratory of Pharmaceutical Biotechnology, Nanjing University, Nanjing, Jiangsu 210023, PR China; Branch of National Clinical Research Center for Orthopedics, Sports Medicine and Rehabilitation, Nanjing, Jiangsu 210008, PR China*

Chenfeng Qiao − *Department of Orthopedics, Jinling Clinical Medical College, Nanjing University of Chinese Medicine, Nanjing, Jiangsu 210002, PR China*

Xiang Gu − *Department of Biomedical Engineering, College of Engineering and Applied Sciences, Nanjing National Laboratory of Microstructures, Jiangsu Key Laboratory of Artificial Functional Materials, Nanjing University, Nanjing, Jiangsu 210023, PR China*

Yuan Liu − *Division of Sports Medicine and Adult Reconstructive Surgery, Department of Orthopedic Surgery, Nanjing Drum Tower Hospital, Affiliated Hospital of Medical School, Nanjing University, Nanjing, Jiangsu 210008, PR China; State Key Laboratory of Pharmaceutical Biotechnology, Nanjing University, Nanjing, Jiangsu 210023, PR China; Branch of National Clinical Research Center for Orthopedics, Sports Medicine and Rehabilitation, Nanjing, Jiangsu 210008, PR China*

Weitong Li − *State Key Laboratory of Pharmaceutical Biotechnology, Nanjing University, Nanjing, Jiangsu 210023, PR China; Branch of National Clinical Research Center for*

https://doi.org/10.1021/acsnano.5c04011
ACS Nano 2025, 19, 23080−23095

Orthopedics, Sports Medicine and Rehabilitation, Nanjing, Jiangsu 210008, PR China; Division of Sports Medicine and Adult Reconstructive Surgery, Department of Orthopedic Surgery, Nanjing Drum Tower Hospital Clinical College of Nanjing University of Chinese Medicine, Nanjing, Jiangsu 210008, PR China

Wenli Gong − *State Key Laboratory of Pharmaceutical Biotechnology, Nanjing University, Nanjing, Jiangsu 210023, PR China; Branch of National Clinical Research Center for Orthopedics, Sports Medicine and Rehabilitation, Nanjing, Jiangsu 210008, PR China; Division of Sports Medicine and Adult Reconstructive Surgery, Department of Orthopedic Surgery, Nanjing Drum Tower Hospital Clinical College of Nanjing University of Chinese Medicine, Nanjing, Jiangsu 210008, PR China*

Zhongyang Lv − *Department of Orthopedics, Nanjing Jinling Hospital, Affiliated Hospital of Medical School, Nanjing University, Nanjing, Jiangsu 210002, PR China*

Yuxiang Fei − *Division of Sports Medicine and Adult Reconstructive Surgery, Department of Orthopedic Surgery, Nanjing Drum Tower Hospital, Affiliated Hospital of Medical School, Nanjing University, Nanjing, Jiangsu 210008, PR China; State Key Laboratory of Pharmaceutical Biotechnology, Nanjing University, Nanjing, Jiangsu 210023, PR China; Branch of National Clinical Research Center for Orthopedics, Sports Medicine and Rehabilitation, Nanjing, Jiangsu 210008, PR China*

Liqian Peng − *State Key Laboratory of Pharmaceutical Biotechnology, Nanjing University, Nanjing, Jiangsu 210023, PR China; Branch of National Clinical Research Center for Orthopedics, Sports Medicine and Rehabilitation, Nanjing, Jiangsu 210008, PR China; Division of Sports Medicine and Adult Reconstructive Surgery, Department of Orthopedic Surgery, Nanjing Drum Tower Hospital Clinical College of Nanjing University of Chinese Medicine, Nanjing, Jiangsu 210008, PR China*

Zhihao Lu − *Division of Sports Medicine and Adult Reconstructive Surgery, Department of Orthopedic Surgery, Nanjing Drum Tower Hospital, Affiliated Hospital of Medical School, Nanjing University, Nanjing, Jiangsu 210008, PR China; State Key Laboratory of Pharmaceutical Biotechnology, Nanjing University, Nanjing, Jiangsu 210023, PR China; Branch of National Clinical Research Center for Orthopedics, Sports Medicine and Rehabilitation, Nanjing, Jiangsu 210008, PR China*

Nuo Xu − *State Key Laboratory of Pharmaceutical Biotechnology, Nanjing University, Nanjing, Jiangsu 210023, PR China; Branch of National Clinical Research Center for Orthopedics, Sports Medicine and Rehabilitation, Nanjing, Jiangsu 210008, PR China; Division of Sports Medicine and Adult Reconstructive Surgery, Department of Orthopedic Surgery, Nanjing Drum Tower Hospital Clinical College of Nanjing University of Chinese Medicine, Nanjing, Jiangsu 210008, PR China*

Chunqing Hu − *Division of Sports Medicine and Adult Reconstructive Surgery, Department of Orthopedic Surgery, Nanjing Drum Tower Hospital, Affiliated Hospital of Medical School, Nanjing University, Nanjing, Jiangsu 210008, PR China; State Key Laboratory of Pharmaceutical Biotechnology, Nanjing University, Nanjing, Jiangsu 210023, PR China; Branch of National Clinical Research Center for Orthopedics, Sports Medicine and Rehabilitation, Nanjing, Jiangsu 210008, PR China*

Hanwen Zhang − *Division of Sports Medicine and Adult Reconstructive Surgery, Department of Orthopedic Surgery, Nanjing Drum Tower Hospital, Affiliated Hospital of Medical School, Nanjing University, Nanjing, Jiangsu 210008, PR China; State Key Laboratory of Pharmaceutical Biotechnology, Nanjing University, Nanjing, Jiangsu 210023, PR China; Branch of National Clinical Research Center for Orthopedics, Sports Medicine and Rehabilitation, Nanjing, Jiangsu 210008, PR China*

Rui Wu − *Division of Sports Medicine and Adult Reconstructive Surgery, Department of Orthopedic Surgery, Nanjing Drum Tower Hospital, Affiliated Hospital of Medical School, Nanjing University, Nanjing, Jiangsu 210008, PR China; State Key Laboratory of Pharmaceutical Biotechnology, Nanjing University, Nanjing, Jiangsu 210023, PR China; Branch of National Clinical Research Center for Orthopedics, Sports Medicine and Rehabilitation, Nanjing, Jiangsu 210008, PR China*

Xingquan Xu − *Division of Sports Medicine and Adult Reconstructive Surgery, Department of Orthopedic Surgery, Nanjing Drum Tower Hospital, Affiliated Hospital of Medical School, Nanjing University, Nanjing, Jiangsu 210008, PR China; State Key Laboratory of Pharmaceutical Biotechnology, Nanjing University, Nanjing, Jiangsu 210023, PR China; Branch of National Clinical Research Center for Orthopedics, Sports Medicine and Rehabilitation, Nanjing, Jiangsu 210008, PR China*

Complete contact information is available at: https://pubs.acs.org/10.1021/acsnano.5c04011

Author Contributions

○J.L. and F.M. are contributed equally to this work. D.Q.S., H.W., Z.Y.S., J.L., F.M., X.Q.X., and R.W. conceived and designed the subject. J.L., Z.Y.S., F.M., C.F.Q., X.G., W.T.L., W.l.G., Z.W., Y.L., Z.Y.L., Y.X.F., C.Q.H., H.W.Z., L.Q.P., N.X., and Z.H.L. performed *in vitro* and *in vivo* experiments. J.L., Z.Y.S., and F.M. analyzed the results. J.L., Z.Y.S., F.M., D.Q.S., and H.W. drafted the manuscript. The manuscript was approved by all of the authors.

Notes

The authors declare no competing financial interest.

ACKNOWLEDGMENTS

This work was supported by the National Science Foundation of China (82325035, 82172481, 32271409), the Six Talent Peaks Project of Jiangsu Province (WSW-079), the Innovation Project of National Orthopedics and Sports Medicine Rehabilitation Clinical Medical Research Center (2021-NCRC-CXJJ-ZH-16).

REFERENCES

(1) Li, W.; Lv, Z.; Wang, P.; Xie, Y.; Sun, W.; Guo, H.; Jin, X.; Liu, Y.; Jiang, R.; Fei, Y.; Tan, G.; Jiang, H.; Wang, X.; Liu, Z.; Wang, Z.; Xu, N.; Gong, W.; Wu, R.; Shi, D. Near Infrared Responsive Gold Nanorods Attenuate Osteoarthritis Progression by Targeting TRPV1. *Adv. Sci.* **2024**, *11* (16), 2307683.

(2) Martel-Pelletier, J.; Barr, A. J.; Cicuttini, F. M.; Conaghan, P. G.; Cooper, C.; Goldring, M. B.; Goldring, S. R.; Jones, G.; Teichtahl, A. J.; Pelletier, J.-P. Osteoarthritis. *Nat. Rev. Dis. Primers* **2016**, *2*, 16072.

(3) Liao, B.; Guan, M.; Tan, Q.; Wang, G.; Zhang, R.; Huang, J.; Liu, M.; Chen, H.; Li, K.; Bai, D.; Zhu, Y. Low-Intensity Pulsed Ultrasound Inhibits Fibroblast-Like Synoviocyte Proliferation and

Reduces Synovial Fibrosis by Regulating Wnt/β-Catenin Signaling. *J. Orthop. Translat.* **2021**, *30*, 41−50.
(4) Hunter, D. J.; March, L.; Chew, M. Osteoarthritis in 2020 and Beyond: a Lancet Commission. *Lancet* **2020**, *396* (10264), 1711−1712.
(5) Gress, K.; Charipova, K.; An, D.; Hasoon, J.; Kaye, A. D.; Paladini, A.; Varrassi, G.; Viswanath, O.; Abd-Elsayed, A.; Urits, I. Treatment Recommendations for Chronic Knee Osteoarthritis. *Best Pract. Res. Clin. Anaesthesiol.* **2020**, *34* (3), 369−382.
(6) Lv, Z.; Yang, Y. X.; Li, J.; Fei, Y.; Guo, H.; Sun, Z.; Lu, J.; Xu, X.; Jiang, Q.; Ikegawa, S.; Shi, D. Molecular Classification of Knee Osteoarthritis. *Front. Cell Dev. Biol.* **2021**, *9*, 725568.
(7) Wang, W.; Duan, J.; Ma, W.; Xia, B.; Liu, F.; Kong, Y.; Li, B.; Zhao, H.; Wang, L.; Li, K.; Li, Y.; Lu, X.; Feng, Z.; Sang, Y.; Li, G.; Xue, H.; Qiu, J.; Liu, H. Trimanganese Tetroxide Nanozyme Protects Cartilage against Degeneration by Reducing Oxidative Stress in Osteoarthritis. *Adv. Sci.* **2023**, *10* (17), No. e2205859.
(8) Collins, J. A.; Kapustina, M.; Bolduc, J. A.; Pike, J. F. W.; Diekman, B. O.; Mix, K.; Chubinskaya, S.; Eroglu, E.; Michel, T.; Poole, L. B.; Furdui, C. M.; Loeser, R. F. Sirtuin 6 (SIRT6) Regulates Redox Homeostasis and Signaling Events in Human Articular Chondrocytes. *Free Radic. Biol. Med.* **2021**, *166*, 90−103.
(9) Ansari, M. Y.; Ahmad, N.; Haqqi, T. M. Oxidative Stress and Inflammation in Osteoarthritis Pathogenesis: Role of Polyphenols. *Biomed. Pharmacother.* **2020**, *129*, 110452.
(10) Lismont, C.; Nordgren, M.; Van Veldhoven, P. P.; Fransen, M. Redox Interplay between Mitochondria and Peroxisomes. *Front. Cell Dev. Biol.* **2015**, *3*, 35.
(11) Kelley, N.; Jeltema, D.; Duan, Y.; He, Y. The NLRP3 Inflammasome: an Overview of Mechanisms of Activation and Regulation. *Int. J. Mol. Sci.* **2019**, *20* (13), 3328.
(12) Dominic, A.; Le, N.-T.; Takahashi, M. Loop between NLRP3 Inflammasome and Reactive Oxygen Species. *Antioxid. Redox Signaling* **2022**, *36* (10−12), 784−796.
(13) Mourmoura, E.; Papathanasiou, I.; Trachana, V.; Konteles, V.; Tsoumpou, A.; Goutas, A.; Papageorgiou, A.-A.; Stefanou, N.; Tsezou, A. Leptin-Depended NLRP3 Inflammasome Activation in Osteoarthritic Chondrocytes Is Mediated by ROS. *Mech. Ageing Dev.* **2022**, *208*, 111730.
(14) Wu, J.; Wang, X.; Wang, Q.; Lou, Z.; Li, S.; Zhu, Y.; Qin, L.; Wei, H. Nanomaterials with Enzyme-Like Characteristics (Nanozymes): Next-Generation Artificial Enzymes (II). *Chem. Soc. Rev.* **2019**, *48* (4), 1004−1076.
(15) Huang, L.; Chen, J.; Gan, L.; Wang, J.; Dong, S. Single-Atom Nanozymes. *Sci. Adv.* **2019**, *5* (5), No. eaav5490.
(16) Tonga, G. Y.; Jeong, Y.; Duncan, B.; Mizuhara, T.; Mout, R.; Das, R.; Kim, S. T.; Yeh, Y.-C.; Yan, B.; Hou, S.; Rotello, V. M. Supramolecular Regulation of Bioorthogonal Catalysis in Cells Using Nanoparticle-Embedded Transition Metal Catalysts. *Nat. Chem.* **2015**, *7* (7), 597−603.
(17) Hou, W.; Ye, C.; Chen, M.; Gao, W.; Xie, X.; Wu, J.; Zhang, K.; Zhang, W.; Zheng, Y.; Cai, X. Excavating Bioactivities of Nanozyme to Remodel Microenvironment for Protecting Chondrocytes and Delaying Osteoarthritis. *Bioact. Mater.* **2021**, *6* (8), 2439−2451.
(18) Zhang, R.; Jiang, B.; Fan, K.; Gao, L.; Yan, X. Designing Nanozymes for *in vivo* Applications. *Nat. Rev. Bioeng.* **2024**, *2* (10), 849−868.
(19) Zhang, Y.; Wei, G.; Liu, W.; Li, T.; Wang, Y.; Zhou, M.; Liu, Y.; Wang, X.; Wei, H. Nanozymes for Nanohealthcare. *Nat. Rev. Methods Primers* **2024**, *4* (1), 36.
(20) Lin, A.; Sun, Z.; Xu, X.; Zhao, S.; Li, J.; Sun, H.; Wang, Q.; Jiang, Q.; Wei, H.; Shi, D. Self-Cascade Uricase/Catalase Mimics Alleviate Acute Gout. *Nano Lett.* **2022**, *22* (1), 508−516.
(21) Koo, S.; Sohn, H. S.; Kim, T. H.; Yang, S.; Jang, S. Y.; Ye, S.; Choi, B.; Kim, S. H.; Park, K. S.; Shin, H. M.; Park, O. K.; Kim, C.; Kang, M.; Soh, M.; Yoo, J.; Kim, D.; Lee, N.; Kim, B.-S.; Jung, Y.; Hyeon, T. Ceria-Vesicle Nanohybrid Therapeutic for Modulation of Innate and Adaptive Immunity in a Collagen-Induced Arthritis Model. *Nat. Nanotechnol.* **2023**, *18* (12), 1502−1514.
(22) Huang, Y.; Ren, J.; Qu, X. Nanozymes: Classification, Catalytic Mechanisms, Activity Regulation, and Applications. *Chem. Rev.* **2019**, *119* (6), 4357−4412.
(23) Liu, Z.; Xie, L.; Qiu, K.; Liao, X.; Rees, T. W.; Zhao, Z.; Ji, L.; Chao, H. An Ultrasmall RuO_2 Nanozyme Exhibiting Multienzyme-Like Activity for the Prevention of Acute Kidney Injury. *ACS Appl. Mater. Interfaces* **2020**, *12* (28), 31205−31216.
(24) Sun, Y.; Mu, S.; Xing, Z.; Guo, J.; Wu, Z.; Yu, F.; Bai, M.; Han, X.; Cheng, C.; Ye, L. Catalase-Mimetic Artificial Biocatalysts with Ru Catalytic Centers for ROS Elimination and Stem-Cell Protection. *Adv. Mater.* **2022**, *34* (46), No. e2206208.
(25) Li, X.; Ren, X.; Xie, M.; Zhu, M.; Zhang, Y.; Li, T.; Huo, M.; Li, Q. Biominerallized Noble Metal-Based RuO_2 Nanozymes against Myocardial Ischemic/Reperfusion Injury. *Adv. NanoBiomed Res.* **2023**, *3*, 2200144.
(26) Chen, Y.; Wei, J.; Wang, L.; Cai, Q.; Yang, F.; Zhang, L.; Liu, J.; Liu, Y. Multi-Enzyme Co-Expressed Ruthenium Dioxide Nanoparticles Activate Mitochondrial Autophagy and Regulate Oxidative Stress for Alzheimer's Disease Treatment. *Chem. Eng. J.* **2024**, *492*, 151868.
(27) Xiong, H.; Zhao, Y.; Xu, Q.; Xie, X.; Wu, J.; Hu, B.; Chen, S.; Cai, X.; Zheng, Y.; Fan, C. Biodegradable Hollow-Structured Nanozymes Modulate Phenotypic Polarization of Macrophages and Relieve Hypoxia for Treatment of Osteoarthritis. *Small* **2022**, *18* (32), No. e2203240.
(28) Wang, X.; Zhong, X.; Lei, H.; Geng, Y.; Zhao, Q.; Gong, F.; Yang, Z.; Dong, Z.; Liu, Z.; Cheng, L. Hollow Cu_2Se Nanozymes for Tumor Photothermal-Catalytic Therapy. *Chem. Mater.* **2019**, *31* (16), 6174−6186.
(29) Dong, S.; Dong, Y.; Liu, B.; Liu, J.; Liu, S.; Zhao, Z.; Li, W.; Tian, B.; Zhao, R.; He, F.; Gai, S.; Xie, Y.; Yang, P.; Zhao, Y. Guiding Transition Metal-Doped Hollow Cerium Tandem Nanozymes with Elaborately Regulated Multi-Enzymatic Activities for Intensive Chemodynamic Therapy. *Adv. Mater.* **2022**, *34* (7), No. e2107054.
(30) Sun, Z.; Muhammad, F.; Qiao, C.; Gong, W.; Wang, Z.; Liu, Y.; Yu, X.; Dong, J.; Lv, J.; Cheng, X.; Lu, Z.; Lin, C.; Lv, Z.; Sun, W.; Yuan, T.; Meng, J.; Wu, R.; Shi, D.; Wei, H.; Bao, N. Templated Synthesis of Hollow RuO_2 Nanospheres for Alleviating Metal Wear Particle-Induced Osteoclast Activation and Bone Loss. *Small* **2025**, *21* (4), No. e2406210.
(31) Muhammad, F.; Chen, X.; Tang, J.; Cheng, Y.; Li, Y.; Zhu, C.; Zhang, Y.; Miao, L.; Deng, Y.; Wei, H. Hydrous Ruthenium Oxide Triggers Template-Free and Spontaneous Growth of Metal Nanostructures. *Chem. Sci.* **2024**, *15* (5), 1679−1691.
(32) Zhang, H.; Lin, C.; Zeng, C.; Wang, Z.; Wang, H.; Lu, J.; Liu, X.; Shao, Y.; Zhao, C.; Pan, J.; Xu, S.; Zhang, Y.; Xie, D.; Cai, D.; Bai, X. Synovial Macrophage M1 Polarisation Exacerbates Experimental Osteoarthritis Partially through R-Spondin-2. *Ann. Rheum. Dis.* **2018**, *77* (10), 1524−1534.
(33) Fernandes, T. L.; Gomoll, A. H.; Lattermann, C.; Hernandez, A. J.; Bueno, D. F.; Amano, M. T. Macrophage: a Potential Target on Cartilage Regeneration. *Front. Immunol.* **2020**, *11*, 111.
(34) Yu, Z.; Lou, R.; Pan, W.; Li, N.; Tang, B. Nanoenzymes in Disease Diagnosis and Therapy. *Chem. Commun.* **2020**, *56* (99), 15513−15524.
(35) Langston, P. K.; Nambu, A.; Jung, J.; Shibata, M.; Aksoylar, H. I.; Lei, J.; Xu, P.; Doan, M. T.; Jiang, H.; MacArthur, M. R.; Gao, X.; Kong, Y.; Chouchani, E. T.; Locasale, J. W.; Snyder, N. W.; Horng, T. Glycerol Phosphate Shuttle Enzyme GPD2 Regulates Macrophage Inflammatory Responses. *Nat. Immunol.* **2019**, *20* (9), 1186−1195.
(36) Chhor, V.; Le Charpentier, T.; Lebon, S.; Oré, M.-V.; Celador, I. L.; Josserand, J.; Degos, V.; Jacotot, E.; Hagberg, H.; Sävman, K.; Mallard, C.; Gressens, P.; Fleiss, B. Characterization of Phenotype Markers and Neuronotoxic Potential of Polarised Primary Picroglia *in vitro*. *Brain Behav. Immun.* **2013**, *32*, 70−85.
(37) Celik, O.; Yildiz, B. O. Obesity and Physical Exercise. *Minerva Endocrinol.* **2021**, *46* (2), 131−144.
(38) Zhang, H.; Wang, L.; Cui, J.; Wang, S.; Han, Y.; Shao, H.; Wang, C.; Hu, Y.; Li, X.; Zhou, Q.; Guo, J.; Zhuang, X.; Sheng, S.;

Zhang, T.; Zhou, D.; Chen, J.; Wang, F.; Gao, Q.; Jing, Y.; Chen, X.; Su, J. Maintaining Hypoxia Environment of Subchondral Bone Alleviates Osteoarthritis Progression. *Sci. Adv.* **2023**, *9* (14), No. eabo7868.
(39) Gross, O.; Poeck, H.; Bscheider, M.; Dostert, C.; Hannesschläger, N.; Endres, S.; Hartmann, G.; Tardivel, A.; Schweighoffer, E.; Tybulewicz, V.; Mocsai, A.; Tschopp, J.; Ruland, J. Syk Kinase Signalling Couples to the Nlrp3 Inflammasome for Anti-Fungal Host Defence. *Nature* **2009**, *459* (7245), 433−436.
(40) Allen, I. C.; Scull, M. A.; Moore, C. B.; Holl, E. K.; McElvania-TeKippe, E.; Taxman, D. J.; Guthrie, E. H.; Pickles, R. J.; Ting, J. P. Y. The NLRP3 Inflammasome Mediates *in vivo* Innate Immunity to Influenza a Virus through Recognition of Viral RNA. *Immunity* **2009**, *30* (4), 556−565.
(41) Franchi, L.; Warner, N.; Viani, K.; Nuñez, G. Function of Nod-Like Receptors in Microbial Recognition and Host Defense. *Immunol. Rev.* **2009**, *227* (1), 106−128.
(42) Fusco, R.; Siracusa, R.; Genovese, T.; Cuzzocrea, S.; Di Paola, R. Focus on the Role of NLRP3 Inflammasome in Diseases. *Int. J. Mol. Sci.* **2020**, *21* (12), 4223.
(43) Bryan, N. B.; Dorfleutner, A.; Rojanasakul, Y.; Stehlik, C. Activation of Inflammasomes Requires Intracellular Redistribution of the Apoptotic Speck-Like Protein Containing a Caspase Recruitment Domain. *J. Immunol.* **2009**, *182* (5), 3173−3182.
(44) Fernandes-Alnemri, T.; Wu, J.; Yu, J. W.; Datta, P.; Miller, B.; Jankowski, W.; Rosenberg, S.; Zhang, J.; Alnemri, E. S. The Pyroptosome: a Supramolecular Assembly of ASC Dimers Mediating Inflammatory Cell Death via Caspase-1 Activation. *Cell Death Differ.* **2007**, *14* (9), 1590−1604.
(45) Jo, E.-K.; Kim, J. K.; Shin, D.-M.; Sasakawa, C. Molecular Mechanisms Regulating NLRP3 Inflammasome Activation. *Cell. Mol. Immunol.* **2016**, *13* (2), 148−159.
(46) Swanson, K. V.; Deng, M.; Ting, J. P. Y. The NLRP3 Inflammasome: Molecular Activation and Regulation to Therapeutics. *Nat. Rev. Immunol.* **2019**, *19* (8), 477−489.
(47) Sun, H.; Sun, Z.; Xu, X.; Lv, Z.; Li, J.; Wu, R.; Fei, Y.; Tan, G.; Liu, Z.; Liu, Y.; Shi, D. Blocking TRPV4 Ameliorates Osteoarthritis by Inhibiting M1 Macrophage Polarization via the ROS/NLRP3 Signaling Pathway. *Antioxidants* **2022**, *11* (12), 2315.

https://doi.org/10.1021/acsnano.5c04011
ACS Nano 2025, 19, 23080−23095